Complex-valued 3D atomic spectroscopy with Gaussian-assisted inline holography

Xing Huang¹, ¹ Yuzhuo Wang^{1,2}, ¹ Jian Zhao¹, ¹ and Saijun Wu¹¹

¹¹Department of Physics, State Key Laboratory of Surface Physics and Key Laboratory of Micro and Nano Photonic Structures (Ministry of Education), Fudan University, Shanghai 200433, China.
²State Key Laboratory of Quantum Optics and Quantum Optics Devices, Institute of Laser Spectroscopy, Shanxi University, Taiyuan 030006, China.

When a laser-cooled atomic sample is optically excited, the envelope of coherent forward scattering can often be decomposed into a few complex Gaussian profiles. The convenience of Gaussian propagation helps addressing key challenges in digital holography. In this work, we theoretically develop and experimentally demonstrate a Gaussian-decomposition-assisted approach to inline holography, for single-shot, simultaneous measurements of absorption and phase shift of small atomic samples sparsely distributed in 3D. Experimentally, we image a sparse lattice of ⁸⁷Rb samples on the D2 line, to resolve their axial positions with micrometer precision, and to retrieve their complex-valued spectroscopic images. With the phase-angle readouts that are highly insensitive to atom-number and interaction-strength uncertainties, we achieve hundred-kHz-level single-shot-resolution to the transition frequency with merely hundreds of atoms. We further demonstrate 3D sensing of local light shift with micrometer spatial resolution.

I. INTRODUCTION

Atoms are ideal quantum sensors. By measuring the optical response of free atoms, the centers and linewidths of atomic levels can be accurately inferred for unveiling unknown interactions and to calibrate external potentials [1–4]. The optical transition properties are affected by the center-of-mass motion. The laser-cooling techniques, which are able to effectively freeze the atomic motion, was expected to greatly enhance the precision of atomic spectroscopy [5]. Nowadays, however, while laser cooling and trapping are often essential in spectroscopic measurements on narrow transitions [6–10], precision spectroscopy on strong transitions tends to rely more on traditional sources such as saturated vapors [11] and atomic beams [12]. Compared to the thermal sources, the fluxes from cold-atom sources are moderate and easily fluctuate. Furthermore, during a prolonged probe period, the light-atom interaction strength, characterized by the atomic polarizability α , can be modified by optical pumping even at extremely low light levels [13]. Efficient suppression of the systematic errors associated with such fluctuations are important for atomic precision spectroscopy to fully benefit from the long-time Dopplerfree interaction offered by laser cooling, and to enable novel applications of ultra-cold atoms such as for wideband quantum sensing of 3D potentials [14–16].

The impacts of atom number and interaction-strength fluctuations can be substantially suppressed in atomic spectroscopy, if one is able to extend the spectroscopic data from real to complex numbers. In particular, for a dilute atomic sample subjected to a near-resonant probe [17], both the optical depth OD and phase shift ϕ are proportional to the atom number N and the modulus of the atomic polarizability $|\alpha|$. But the phase angle $\beta = \arg(\phi + i\mathrm{OD}/2)$ is largely decided by the atomic phase angle, $\arg(\alpha)$, highly insensitive to the $N|\alpha|$ fluctuations [18, 19]. Unfortunately, it is not possible to simultaneously measure OD and ϕ distributions

without precisely knowing the complex E'_r and E_r , the transmitted probe wavefronts in presence and absence of the atomic sample respectively. In standard transmission imaging techniques where the light intensities are recorded only [17, 20], the optical phase information are completely lost. While single-mode coherent transmission spectroscopy [21–24] is able to retrieve the E_r -mode-averaged OD and ϕ , the single-mode readouts cannot support spatial resolution in general. Furthermore, since details of atomic distribution are disregarded, it becomes difficult to correct for any density-dependent shifts in the collective responses [25–27].

In this work, we develop a systematic procedure for complex-valued spectroscopic imaging of laser-cooled The technique is based on inline holography [18, 19, 28–30]. To fix the optical phase ambiguity [31] by exploiting the prior knowledge about the atoms in a numerically efficient manner, we introduce a Gaussian-decomposition [32–34] method to digital holographic microscopy. For arrays of samples with known phase angle β , our method is able to retrieve the transmitted E'_r (and E_r) from single-shot hologram data while spectroscopically locating the centers of each sample in 3D with a super-resolution close to the photon-shotnoise limit (Cramer-Rao bound [35]). The absorption OD and phase-shift ϕ images can be numerically reconstructed to form the complex $\varphi_A = \phi + iOD/2$ images, with diffraction-limited spatial resolution and photonshot-noise limited sensitivity. Experimentally, we simultaneously reconstruct complex-valued spectroscopic images of sparsely distributed ⁸⁷Rb samples on the D2 line, from single-shot holograms which are recorded within tens of microseconds. By retrieving the phase angles, we demonstrate 100 kHz-level resolution to the transition frequency and its shift using merely hundreds of atoms, with micrometer-level 3D spatial resolution, in presence of substantial shot-to-shot atom-number uncertainties.

In what follows, we first review the basic principles of the quantitative holographic imaging [36–38] for atomic

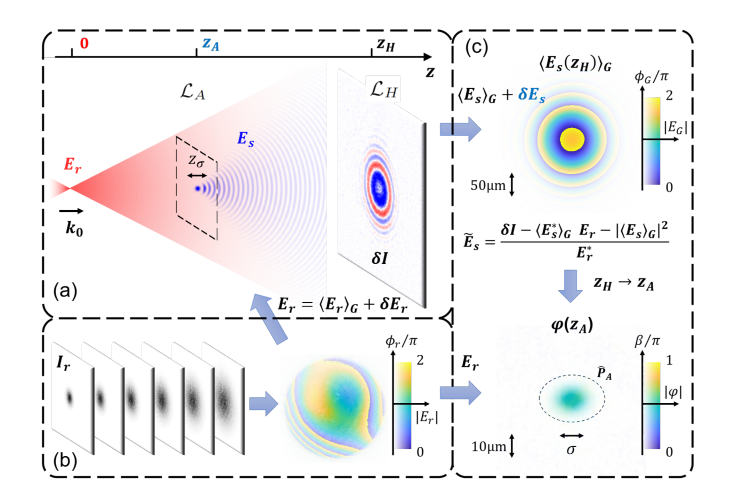


FIG. 1. Complex spectroscopic imaging with Gaussiandecomposition-assisted inline holography. (a): The basic setup. (b): Pre-characterization of the reference field $E_r =$ $\sqrt{I_r}e^{i\phi_r}$ through multi-plane intensity $I_r = |E_r|^2$ measurements [18]. The low-spatial-frequency part of the forward scattering $E_s = E'_r - E_r$ is decomposed into multiple Gaussian profiles according to Eq. (7). The Gaussian propagation supports efficient minimization of \mathcal{L}_H associated with the $\delta I = I' - I$ data in the camera plane $z = z_H$, and \mathcal{L}_A associated with the sample knowledge around $z = z_A$, according to Eq. (10). (c): The full E_s , approximated by \tilde{E}_s in Eq. (13), is propagated together with E_r to $z=z_A$ to retrieve the complex phase shift $\varphi(z_A)$ as the complex-valued imaging data. The scale bars are according to typical experimental condition in this work. The (colored) black symbols refer to quantities that are (not) precisely known at the represented stages of measurements.

spectroscopy [18]. We then introduce our new method where Gaussian decomposition [32–34] is applied into holography, to facilitate the phase retrieval and 3D localization of atomic samples.

A. Complex-valued imaging with inline holography

We consider the inline holography setup [29, 31] illustrated in Fig. 1a where a nearly spherical atomic sample at $z=z_A$, with a characteristic width σ , is resonantly excited by a spherical probe beam E_r with optical frequency ω , wavelength λ and wavenumber $k_0=2\pi/\lambda$. The attenuation and phase shift to E_r is encode in E_s , the coherent forward scattering from the sample. We therefore rewrite $E'_r=E_r+E_s$. Defining [39]

$$\varphi(z) = -i\log(1 + E_s(z)/E_r(z)),\tag{1}$$

then, according to Beer-Lambert law, we have the complex phase shift by the sample [18]

$$\varphi_{A}(x,y) = \varphi(x,y,z_{A}),$$

$$= \phi(x,y) + i\text{OD}(x,y)/2,$$

$$\approx \frac{1}{2}k_{0}\rho_{c}(x,y)\alpha(\omega).$$
(2)

Here $\rho_c = \int \rho(z) dz$ is the column density. The $\alpha(\omega)$ is the atomic polarizability. The third line in Eq. (2) becomes accurate for small ensemble of dilute atoms with $k_0^3 \rho \ll 1$.

The transmitted E_r, E_r' propagate further for a distance $z_H - z_A$ where the intensity is recorded by a digital camera. The intensities in presence and absence of the atomic sample are modeled as

$$I' = |E_r(z_H) + E_s(z_H)|^2,$$

$$I = |E_r(z_H)|^2,$$
(3)

respectively. The reduced hologram is defined as

$$\delta I = I' - I. \tag{4}$$

Assuming the probe profile E_r as known, the goal of holographic imaging is to infer through the I', I measurements the axial central location z_A and to retrieve the 2D complex phase shift image $\varphi_A(x, y)$ (Eq. (2)) there.

B. Challenges

The quantitative holographic imaging technique [36–38] faces at least three categories of challenges, which are all amplified in cold atom setups [18, 19, 30, 40–43]:

C1: To retrieve E_s from the I', I data with Eq. (3) is an ill-defined problem, requiring additional constraints to fix the E_s solution not to be perturbed by its twin [31],

$$E_{s,\text{twin}} = \frac{E_r}{E_r^*} E_s^* \tag{5}$$

at $z = z_H$, which focuses approximately at

$$z_{\text{twin}} = \frac{z_A z_H}{2z_A - z_H}. (6)$$

Due to the fragile nature of cold atomic samples and typical complexity of the setup that produce them, traditional solutions to the twin-image problem associated with phase-shifting [44] and multiple phase-diversity measurements [45–47] can not be easily implemented. While off-axes holography [40, 42, 48] is powerful for resolving the optical phase, the technique necessarily sacrifices some of the imaging bandwidth while adding more complexity to the setup. Finally, while structured illumination [49] may help solving the phase problem, the associated E_r structure could complicate the light-atom interaction through Doppler shifts and transition saturation [13].

Without resorting to additional measurements, the constraints available for cold atom holography typically only include those associated with finite spatial support [18, 30, 40, 42] and optical response characteristics [41, 43]. Previous applications of these prior knowledge, while leading to notable successes, may still not guarantee an accuracy for precision spectroscopy in presence of imaging noises.

C2: The sample plane location z_A is not known a prior for the numerical back-propagation of the reconstructed E_r , E_s [19, 42]. Retrieving OD and ϕ with the Eqs. (1)(2) relation in an out-of-focus plane mixes the absorption with phase shift [50, 51], leading to erroneous phase angle β .

Cold atoms in a dilute enough gas typically follow a normal density distribution. The lack of distinct spatial features invalidates a class of traditional methods for sample-plane localization in digital holography [52–56]. While the sample plane can be precisely located by observing the atomic shot noise [43], the method is slow since many images are required for the statistical analysis.

C3: While the E_r wavefront is assumed known, any deviation of the actual E_r induces distortion to the retrieved E_s , leading to erroneous φ_A . In particular, the speckle noises [57] in E_r can hardly be avoided in atomic spectroscopy where the laser probe is necessarily monochromatic [18, 30].

C. This work

We develop a method for complex-valued spectroscopic imaging of sparsely distributed atomic samples in 3D. As outlined in Fig. 1, the method is based on inline holography [28]. The phase ambiguity associated with the twin image (Eq. (5)) is addressed by systematically exploiting our prior knowledge about the measurement. Apart from the hologram data (Eq. (3)), the pre-characterized E_r wavefront [18], our prior knowledge is mostly about the bulk optical properties of the samples in focus, *i.e.*, aspects of the complex phase shift profile $\varphi_A(x,y)$ at $z = z_A$. The key insight is that when the probe beam E_r seen by the sample is locally smooth, then these properties can be efficiently parametrized by decomposing E_s into a few Gaussian beams (see Eq. (B7)) [32–34],

$$E_G(\mathbf{r}; \{c_j, \mathbf{P}_j\}) = \sum_{j=1}^{n_A} c_j G_j(\mathbf{r}; \mathbf{P}_j). \tag{7}$$

We denote the optimal decomposition as $\langle E_s \rangle_G = E_G(\mathbf{r}; \{c_j, \mathbf{P}_j\}_{\text{opt}})$. The Gaussian propagation facilitates simultaneous minimization of cost functions, \mathcal{L}_H at $z = z_H$ (Eq. (11)) associated with the I', I-data, and \mathcal{L}_A at $z = z_A$ (Eq. (12)) associated with the expected φ_A .

Our method works especially well in a "defocused twin regime" (Appendix C1) for small atomic samples, with $z_{\sigma} \ll z_A, z_H - z_A$, so that there are sufficient interference fringes in the I'-data (Eq. (4)). Here $z_{\sigma} = \pi \sigma^2/\lambda$ is the characteristic Rayleigh length of the sample. Key advantages of our method is summarized as follows:

A1: Our method generalizes traditional single-shot twin-removal strategies such as those associated with finite spatial supports [30, 58, 59] and spectral phase angles [41, 60]. Here, bulk properties

of the samples such as the approximate 3D locations, shapes, and spatial-(in)dependent spectral responses, can all be encoded into the φ_A -image-expectations to constrain the $\{c_j, \mathbf{P}_j\}$ parameters. The enhanced application of prior knowledge improves the accuracy of the optical phase determination in presence of imaging noises.

A2: With the phase angle $\beta = \arg(\varphi_A)$ constrained by knowledge of light-atom interaction [19, 41, 43], the atomic sample plane location z_A can be conveniently inferred during Gaussian decomposition. For nearly spherical samples with $z_{\sigma} \ll z_A, z_H - z_A$, the typical axial resolution is [19] (Appendix A)

$$\Delta z_A \approx z_\sigma / \sqrt{N_s},$$
 (8)

decided by the Rayleigh length $z_{\sigma} = \pi \sigma^2/\lambda$ associated with the sample size σ (Fig. 1a). This resolution can be enhanced by introducing finer sample features, or simply by repeating the in situ measurements with standard samples to effectively increase the total number of coherently scattered photons $N_s = \sum_{x,y} |E_s|^2$ received by the camera.

A3: With $z_{\sigma} \ll z_A, z_H - z_A$, diffraction-limited E_r and E_s can be retrieved from single-shot I', I data, using the pre-characterized E_r knowledge through multi-plane intensity measurements [18]. Impacts of mild speckle noises and moderate aberrations can be corrected, for achieving complex $\varphi_A(x,y)$ imaging with diffraction-limited resolution and photon-shot-noise limited sensitivity. The phase-angle resolution is given by [18] (Appendix A)

$$\Delta \beta(\mathcal{A}) \approx 1/\sqrt{2N_s(\mathcal{A})}.$$
 (9)

Here $N_s(\mathcal{A}) = \sum_{\mathcal{A}} |E_s|^2$ integrates the elastically scattered photons over area \mathcal{A} of interest in the infocus $\varphi_A(x,y)$ image.

1. Application to atomic spectroscopic imaging

With the inclusion of both phase-angle β and modulus $|\varphi_A|$ readouts into the spectroscopy data, the previously mentioned challenges in cold atom spectroscopy—stemming from fluctuations in atom number and interaction strength—become significantly more manageable. When combined with 3D imaging capabilities, our complex spectroscopy technique substantially improves the potential for imaging and sensing on strong optical transitions with laser-cooled atomic arrays.

It is important to note that compared to absorption [17] or phase contrast [20] techniques, holographic imaging incurs a 50% loss of information [30, 40] (see Appendix A). In the following, we argue that such a loss hardly disadvantages our single-shot complex spectroscopic approach in precision measurements.

To start with, our method avoids measurement noises associated with atom-number and interaction-strength normalization, which, except for special kind of samples with known atom number and fixed interaction strength [61], is typically required in precision spectroscopy [62]. To see the potential of holographic complex imaging at the fundamental level, we compare a special case of resonant absorption and holographic imaging, i.e., with the probe beam frequency ω tuned close to the transition frequency ω_{eq} so that the sample is absorptive. It is easy to show that compared to a double-shot absorption measurement, including one for atom-number and interaction-strength normalization (assuming as being performed perfectly), the holographic signals from two independent measurements support just the same, photon-shot-noise-limited absorption sensitivity.

Furthermore, the holographic measurement obtains the absorption and phase-shift image at the same time. The complex-valued spectroscopy is Δ -sensitive at any detuning $\Delta = \omega - \omega_{eg}$. Near resonance, the absorption or fluorescence profiles are peaked and therefore lose the detuning-sensitivity to the first order. In contrast, on-resonance our complex spectroscopy achieves the best sensitivity, capable of resolving ω_{eg} within single shot through the phase-angle β measurement. In the limit of low density [25] and/or high probe intensity [63], the phase angle β is purely decided by the single-atom response [19], ideal for precision spectroscopy. Furthermore, with diffraction and shot-noise limited OD, ϕ image data, minimal modeling of atomic distributions supports correction to density-dependent shifts [25].

Finally, it is worth noting that phase-angle spectroscopy can be substantially more robust against power broadening and optical pumping effects (Sec. IID) [19] than those in regular spectroscopy. This, combined with the fact that the complex-valued spectroscopy does not require the sample to be nearly intact for the normalization later, suggesting that more efficient precision measurements are possible without requiring extremely low light-level operations [13, 62].

2. Major limitations in this work

Practically, our holographic imaging method [18] can be conveniently adapted to standard imaging setups, simply by translating the camera away from the atomic imaging plane for recording the inline interference patterns (Fig. 1a). Numerically, a key step is based on matching E_r, E_s with free-propagating Gaussian beams through the nonlinear minimization of Eq. (10). The method helps to overcome several major obstacles in quantitative holography, but also introduces substantial limitations. In the following we discuss major limitations and possible improvements.

First, the nonlinear optimization is quite slow. As we find in this work, while the analytical form of the Gaussian beam (Eq. (B7)) [32–34] helps to avoid the

resource-demanding, numerical propagation of full wavefronts [18, 30, 42, 43], to resolve single hologram still requires about 2 minutes even with a A100 GPU card (NVIDIA). Notably, for repeated measurements such as during a probe-frequency scan [1, 62], the processing time can be substantially reduced, down to tens of seconds, by seeding the optimization process with nearly optimal initial $\{c_j, \mathbf{P}_j\}$ -parameters. With more advanced software and hardware supports, we expect further improved imaging processing speed in future work.

Second, as detailed in Appendix C1, diffractionlimited $\varphi(z_A)$ -image is most easily achieved for small samples satisfying $z_{\sigma} \ll z_A, z_H - z_A$ (Fig. 1a) only. Beyond this "defocused-twin regime", accurate φ_A -retrieval relies on improving the decomposition of E_s using more Gaussian profiles (larger n_A), i.e., to capture fine details of E_s so that the defocused twin-image noise (Eq. (13)) around $z = z_A$ is more efficiently removed. While the principle of such improvement as outlined in Sec. IIB appears straightforward, its practicality in presence of imaging noise requires systematic study in future work. Nevertheless, we note that depending on the spatial resolution requirements, the z_A and $z_H - z_A$ limited by the camera sensor size can typically be at a centimeter level. This in term supports sparse arrays with individual sample size of up to 100 μ m (Fig. 6), large enough for various applications. At moderate z_{σ} , the Gaussian-decomposition method can also be assisted by Gerchberg-Saxton-type iterations [18, 29, 30, 58] to improve the E_s estimation.

Finally, the Gaussian-assisted holography method in this work assumes free-propagation between the sample plane at $z = z_A$ and camera plane at $z = z_H$. Practically, the atomic samples are often imaged to the camera plane through a lens array [17, 43, 64]. In this experimental work, the moderate, aplanatic aberrations in E_s are corrected by a pre-characterized point-spread-function near the atomic sample location (Appendix D3). Obviously, the method becomes insufficient in presence of strong astigmatism during, e.g., wide-field imaging [65–67]. In future work and with sufficient knowledge of the imaging system, full suppression of strong, astigmatic aberrations can be achieved by exploiting the Gaussian propagation across the lens array numerically [33, 34]. This may potentially enable diffraction-limited 3D complex-valued spectroscopic imaging across unprecedented imaging volumes, only limited by the pixel-size of the camera [68].

D. Structure of the rest of the paper

In the following the main text is structured into three sections. With technical details presented in Appendix B, we first outline the principles of the Gaussian-decomposition-assisted holographic imaging method in Sec. II. Next, in Sec. III we present experimental demonstration of diffraction and shot-noise limited complex-valued imaging. We summarize this work in Sec. IV.

II. PRINCIPLES

The schematic setup of our Gaussian-decomposition-assisted complex-valued spectroscopic imaging method is illustrated in Fig. 1(a-c). The Fig. 1a setup is already outlined in Sec. IA. We regard the (I',I) measurement as a single-shot measurement. With in mind no atom-number or interaction-strength normalization measurement is required later, the I'-exposure can be strong and elongated to substantially alter the atomic velocity and/or the internal atomic state population. The I-exposure is taken immediately after the atomic sample is dispersed from the E_r illumination.

We assume the holographic imaging setup to be effectively lensless [30] so that the accurate propagation of wavefronts between z_A and z_H is modeled by Eq. (D1), $E(z') = \hat{U}(z'-z)E(z)$, through angular spectrum method numerically. On the other hand, for repetitive short-distance propagation during numerical optimization, the Gaussian-decomposed E_r, E_s wavefronts are sampled according to the analytical Eq. (B7) under paraxial approximation (also see Appendix D 3.).

The reconstruction of $\varphi_A(x,y)$ at $z=z_A$ is divided into Sec. II A, II B, II C steps.

A. Obtaining E_r

A prerequisite to recover E_s through the holographic measurement with Eq. (3) is to characterize the E_r wavefront precisely. The steps for the E_r measurements are illustrated in Fig. 1(a,b), detailed in ref. [18]. Briefly, using the single-shot I-data, the probe wavefront $E_r = \sqrt{I}e^{i\phi_r}$ is obtained by intensity-matching I to $I_0 = |E_r^{(0)}(z_H)|^2$. Here $\phi_r = \arg(E_r^{(0)})$. $E_r^{(0)}$ is the pre-characterized probe wavefront, obtained with multi-plane intensity measurements of E_r , followed by Gerchberg-Saxton iteration [69] (Fig. 1b). Notice the E_r wavefront measurement is designed to share the same optical path with the holographic measurement.

B. Minimal Gaussian-decomposition of E_s

We parametrize E_s with n_A Gaussian beams according to Eq. (7), and minimize the cost function

$$\mathcal{L}_{\text{tot}}(z_A, \{c_i, \mathbf{P}_i\}) = \mathcal{L}_H + \mathcal{L}_A, \tag{10}$$

with

$$\mathcal{L}_{H}(\{c_{j}, \mathbf{P}_{j}\}) = \sum_{x,y} \left| \delta I - E_{r}^{*} E_{G} - E_{r} E_{G}^{*} - |E_{G}|^{2} \right|^{2},$$
(11)

and

$$\mathcal{L}_{A}(z_{A}, \{c_{j}, \mathbf{P}_{j}\}) = \sum_{\mu} m_{\mu} C_{\mu} \left(\varphi_{G}(z_{A}, \{c_{j}, \mathbf{P}_{j}\}) \right).$$
 (12)

Here \mathcal{L}_A is formulated into a list of C_μ -constraints (Appendix B 2) weighted by m_μ , which can be adjusted during the optimization. The $\varphi_G(z_A; \{c_j, \mathbf{P}_j\}) = -i\log\left(1 + E_G/\langle E_r\rangle_G\right)_{z=z_A}$ evaluates the complex-valued phase shift by Eq. (1), with E_r replaced by the known Gaussian envelope $E_r \approx \langle E_r\rangle_G$. Simultaneous evaluation of Eq. (11) at $z=z_H$ and (12) with varying z_A is assisted by the analytical Gaussian propagation (Eq. (B7)).

We assume the envelope $\langle E_s \rangle_G$ to be sparse in the Gaussian beam basis. To ensure a minimal n_A for the E_s decomposition, we start with $n_A=1$ in Eq. (7) for each atomic sample and progressively increase n_A by splitting one of the optimal Gaussian beams for additional optimization. During the process, the quality of the decomposition is checked by analyzing the difference between $\langle E_s(z_A)\rangle_G$ with the $\tilde{E}_s(z_A)$ approximation,

$$\tilde{E}_s(z_A) = \hat{U}(z_A - z_H)\tilde{E}_s(z_H), \text{ with}$$

$$\tilde{E}_s(z_H) = \left(\frac{\delta I - E_r \langle E_s \rangle_G^* - |\langle E_s \rangle_G|^2}{E_r^*}\right)_{z=z_H}$$
(13)

as

$$\delta E_G(z_A) = \tilde{E}_s(z_A) - \langle E_s(z_A) \rangle_G. \tag{14}$$

Here the Gaussian approximation $\langle E_s(z_A)\rangle_G$ only contains low-spatial-frequency part of $E_s(z_A)$. $\tilde{E}_s(z_A)$ has the full imaging bandwidth, except that with the twin (Eq. (5)) and a typically weaker "dc" $|E_s|^2/E_r^*$ approximately removed, $\tilde{E}_s(z_A)$ is subjected to disturbance by high-frequency residual of $E_{s,\text{twin}}$ not captured by the Gaussian approximation. In principle, the optimization should continue until sufficient n_A Gaussians ensures fine enough decomposition, so that the $\delta E_G(z_A)$ in Eq. (14) becomes featureless, i.e., the two approximations agree at low-spatial-frequency of interest. In this work, the decomposition process is terminated emphatically (Sec. III) at $n_A = 3$ for small spherical samples (See Appendix E for larger n_A examples). We expect more systematic study in future work on the refinement of $\langle E_s \rangle_G$ decomposition, particularly for large samples.

Finally, the above analysis is easily generated to multiple samples, indexed by A, which are centered at $\mathbf{r}_A = \{x_A, y_A, z_A\}$ to be sparse enough (Appendix C2) not to interfere with each other during the Gaussian decomposition. We refer the coherent forward scattering by each sample as $E_{s,A}$ so that $E_s = \sum_A E_{s,A}$.

C. Retrieving diffraction-limited φ_A

When the constrained Gaussian-decomposition to E_s is successful, an estimation of the Gaussian envelop $\langle E_s \rangle_G$ is obtained. Depending on the prior knowledge of the phase angle β , the sample plane location $z = z_A$ is determined with an accuracy close to the photon-shot-noise limit (Eq. (8)) (Appendix A). We therefore obtain the low-resolution envelop of the complex-valued phase-shift,

$$\langle \varphi_A \rangle_G = -i \log \left(1 + \langle E_{s,A} \rangle_G / \langle E_r \rangle_G \right)_{z=z_A}.$$
 (15)

When $z_{\sigma} \ll z_A, z_H - z_A$, the low-resolution reconstruction of $\langle \varphi_A \rangle_G$ can be refined into diffraction-limited φ_A image according to Eq. (1), simply by replacing the E_s there with

$$E_{s,A}(z_A) \approx \hat{P}_A\left(\tilde{E}_s(z_A)\right),$$
 (16)

where

$$E_r(z_A) = \hat{U}(z_A - z_H)E_r(z_H).$$
 (17)

The z_A localization can be accordingly refined. The aperture operator \hat{P}_A encloses a minimal area at $z = z_A$, according to our prior knowledge about the sample location (Fig. 1c), to select the $E_{s,A}$ wavefront.

As to be explained in Appendix C1, $E_s(z_A)$ contains all E_s features within the full imaging bandwidth, except that it is subjected to disturbance by the out-of-focus, high-frequency-part of $E_{s,\text{twin}}$ not captured by the Gaussian approximation. By operating the Fig. 1a setup in the "defocused-twin regime" with $z_{\sigma} \ll z_A, z_H - z_A$, the residuals spread out sufficiently not to affect the φ_A retrieval. In addition, Eq. (16) assumes that the multiple samples are only weakly displaced along z, as in this experimental work, with coherent forward scattering not overlapping in the sample planes. To retrieve φ_A for multiple samples with substantial $E_{s,A}$ overlap requires separation of each $E_{s,A}$ in a self-consistent manner, a scenario that will be discussed in Appendix C 2.

D. Complex phase shift near an isolated transition

The φ_A measurement as outlined above needs to be compared with theory to extract useful information. With Eq. (2) and for small and dilute ensemble of atoms in the Beer-Lambert regime, the transmission of probe light is purely decided by the complex phase shift $\varphi_A(x,y) \propto \rho_c(x,y)\alpha$ associated with moderate absorption OD and phase shift ϕ . For weak and short enough probe, the linear response α can be evaluated by firstorder perturbation theory [70]. However, when applying the formula to real experiments, the accuracy of the estimation is often prone to optical saturation [13] and multi-scattering [25] effects. A closer look into the transient atomic response suggests that even for fairly strong probe, e.g., either for suppressing multi-scattering effects [63, 71] or for enhancing the signal, the complex phase φ_A can often still be approximated by [19]

$$\varphi_A(x,y) \approx \xi(s_0, \Delta) \frac{3}{8\pi} \rho_c(x,y) \lambda^2 \frac{-\Gamma/2}{\Delta + i\Gamma/2}.$$
 (18)

Here s_0 is the probe saturation parameter. The $\Delta = \omega - \omega_{eg}$ is the probe detuning from the isolated ω_{eg} atomic resonance under study. Γ is the linewidth. The real number $\xi(s_0, \Delta)$ is a saturation factor associated with internal state dynamics. For example, for long enough probe to a closed transition so that the atomic response

is able to reach its steady state, we have the standard $\xi(s_0, \Delta) \approx C^2/(1+s)$ associated with the coherent dipolar excitation, with $C^2 \leq 1$ decided by the probe polarization and optical-pumping induced atomic population re-distribution, and $s = s_0 \Gamma^2/(4\Delta^2 + \Gamma^2)$ [72].

As detailed in ref. [19], the Eq. (18) approximation is valid for smooth and long probe pulse with duration $\tau_p \gg 1/\Gamma$ so that transient effects can be averaged out, and for spectrally isolated g-e transition so that virtual mixing to distant levels is ineffective [19]. Clearly, in Eq. (18) the $\xi(s_0, \Delta)$ factor dictates the power-broadening in OD = $2\text{Im}[\varphi_A]$ and $\phi = \text{Re}[\varphi_A]$. But the phase angle $\beta = \arg[\varphi_A]$ is intact even for $s \gg 1$. The robust phase-angle relation is exploited to axially locate the z_A plane (Appendix B 2 b, B 2 c) [19]. Nevertheless, one should be cautious that apart from transition shifts and broadening associated with mixing distant levels [19], the $\Delta' = \Delta - k_0 \overline{\Delta v}$ is also shifted from Δ by atomic motion along the probe wavevector \mathbf{k}_0 , which can be induced by radiation pressure during prolonged excitation of free atoms.

III. EXPERIMENTAL DEMONSTRATION

In this section, we demonstrate 3D complex-valued spectroscopic imaging of laser-cooled ⁸⁷Rb samples on the D2 line. The energy diagram is given in Fig. 2a. The D2 linewidth is $\Gamma = 2\pi \times 6$ MHz [72].

A. Experimental setup

The schematic setup is illustrated in Fig. 2a. The probe beam is generated by an NA = 0.3 objective [73] to create a diffraction-limited focus at z = 0 in vacuum. A sparse array of ⁸⁷Rb atoms is created around $z_A \approx 1.5$ mm, as to be detailed in the following. During holographic imaging, the E_r, E_s wavefronts are relayed by an aberration-compensated D = 50.8 mm-diameter lens-array [74], not shown in the figure, to the camera (PICO Pixelfly-USB) sensor outside the vacuum. The imaging system has a reduced numerical aperture of NA = 0.26, limited by additional optics following the objective, and a lateral magnification of M=3.5. To perform inline holography, the camera is translated along z, defocused by $\Delta z_H^{(0)} = 17.5$ mm, to record the magnified I', I holograms. In the following and for the convenience of presentation, we describe the imaging process in-situ, as in Fig. 2a, where the camera plane is effectively at z_H that is displaced from z_A by $\Delta z_H^{(0)}/M^2 \approx 1.4$ mm. We refer readers to Sec. IV A and Appendix D 3 where steps for aberration corrections are discussed.

We construct a 3D optical lattice, as in Fig. 2a, to confine a sparse atomic sample array. The lattice geometry is adapted to the limited optical access in our setup. Two of the five lattice beams, propagating along $\tilde{\mathbf{e}}_x = \frac{1}{\sqrt{2}}(\mathbf{e}_x + \mathbf{e}_y)$ with a 3° intersecting angle, creates

1D lattice along the $\tilde{\mathbf{e}}_y = \frac{1}{\sqrt{2}}(\mathbf{e}_x - \mathbf{e}_y)$ direction. Three other beams propagate along $\tilde{\mathbf{e}}_y$ to form a square lattice in the $\{\tilde{\mathbf{e}}_x, \mathbf{e}_z\}$ plane. The primitive lattice vectors are oriented along the $\frac{1}{\sqrt{2}}(\tilde{\mathbf{e}}_x \pm \mathbf{e}_z)$ directions. A relative frequency shift of 20 MHz between the two $\tilde{\mathbf{e}}_x$ -beams and the three $\tilde{\mathbf{e}}_y$ -beams removes the interference between the two lattice confinement dimensions.

We choose the lattice laser wavelength to be $\lambda_l =$ 779.5 nm, blue-detuned from the rubidium D2 line. With $\sim 100 \text{ mW}$ per beam, 10 mK-level trapping potentials are formed for the ground-state rubidium atoms around the dark centers of lattices. The lattice constants along $\tilde{\mathbf{e}}_{u}$ and in the $\tilde{\mathbf{e}}_x - \mathbf{e}_z$ plane are $15\mu\mathrm{m}$, $18\mu\mathrm{m}$ and $22\mu\mathrm{m}$, respectively. Following a gray molasses cooling stage [75], ⁸⁷Rb from a magneto-optical trap is loaded directly into the lattices, resulting in samples with a characteristic width of $\sigma \approx 2.5 \ \mu \text{m}$ and typical atom number of $10^2 \sim 10^3$ per site with $\rho = 10^{12} \sim 10^{13}/\text{cm}^3$ in density. Observing these samples along z, the transverse displacements between adjacent samples are about 10 μ m, well resolvable with our coherent imaging resolution of $\delta x =$ $\lambda/NA = 3 \mu m$. Here $\lambda = 780 \text{ nm}$. On the other hand, the axial displacement of $\delta z = 10 \,\mu\mathrm{m}$ is below the diffractionlimited resolution of $(\delta z)_{\rm res} = 2\lambda/{\rm NA}^2 = 23 \ \mu{\rm m}$.

To perform atomic spectroscopy, we release the atomic samples from the optical lattices and then immediately fire a $\tau_{\rm p}=20~\mu{\rm s}$ probe pulse. The probe polarization is along ${\bf e}_x$. The local intensity of 3 mW/cm² leads to $s_0\approx 1$ saturation parameter in this work for the $\pi-{\rm excitation}$ of unpolarized atoms. In repeated experiments we scan the probe detuning $\Delta=\omega-\omega_{eg}$ across the D2 hyperfine F=2-F'=3 transition. Up to 9 holograms are taken at each detuning. A typical reduced hologram, $\delta I=I'-I$, is given in Fig. 2c, taken on resonance with $\Delta\approx 0$.

B. Results

With the $\{I',I\}$ -hologram set and the precharacterized E_r , We follow the procedure outlined in Sec. II to reconstruct E_s using the Gaussian-decomposition method. To initiate the nonlinear optimization (Eq. (10)), we first directly propagate $E_s^{(0)} = \delta I/E_r^*$ to an estimated atomic sample plane \bar{z}_A . As evident from Eq. (3), with this step $E_s(\bar{z}_A)$ can be focused, albeit being contaminated by a weak, defocused background associated with the "twin" term $E_{s,\text{twin}}$ (Eq. (5)), as well as a typically even weaker "dc" $|E_s|^2/E_r^*$ term. Nevertheless, the preliminary $E_s^{(0)}(\bar{z}_A)$ image in Fig. 2b helps us to initialize the $\{c_j, \mathbf{P}_j\}$ -parameter and compute $E_G^{(0)}$, as in Fig. 2d, with which we evaluate the expected (reduced) hologram $\delta I_e^{(0)} = E_r^* E_G^{(0)} + E_r E_G^{(0)^*} + |E_G^{(0)}|^2$ in Fig. 2e. As by Eq. (10), the minimization of $\mathcal{L}_{\text{total}}$ involves

As by Eq. (10), the minimization of $\mathcal{L}_{\text{total}}$ involves simultaneous minimization of $\mathcal{L}_H = \sum |\delta I_e - \delta I|^2$ and a set of $\mathcal{C}_{\mu}(\varphi(z_A))$ in \mathcal{L}_A associated with the expected φ_A distribution. In this step, we exploit spatial (Ap-

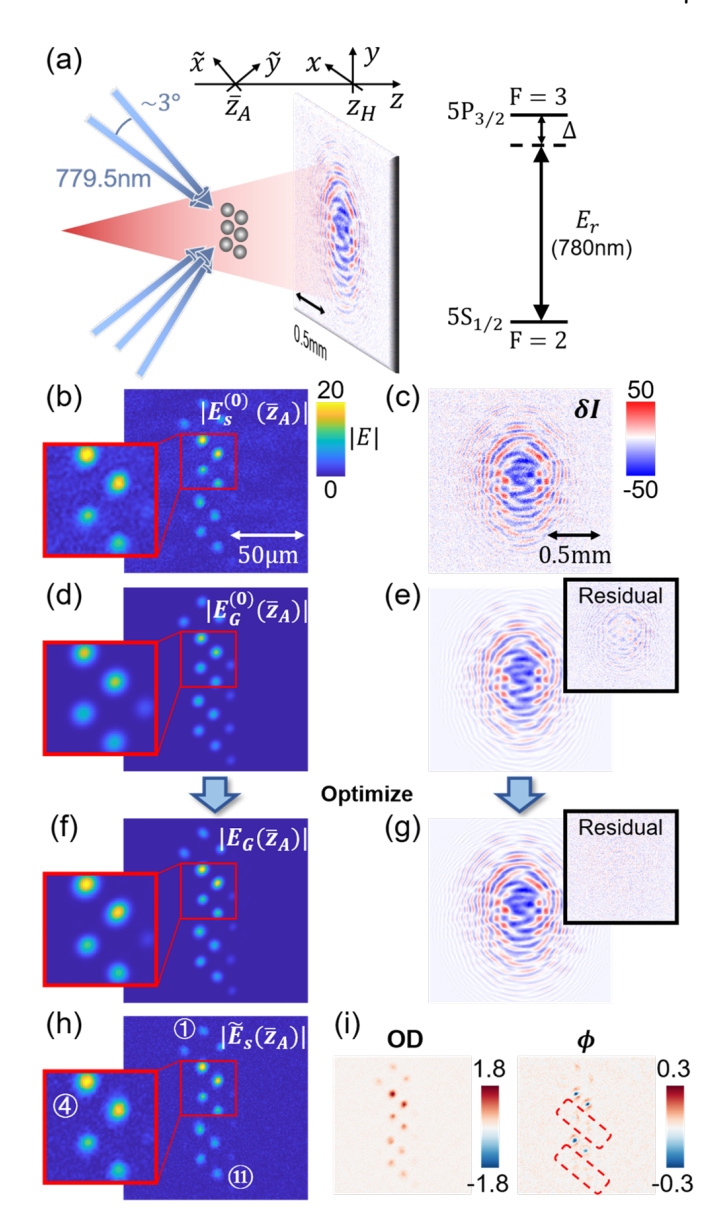


FIG. 2. (a): Sketch of the experimental setup, typical hologram δI at $\Delta \approx 0$, and the atomic level diagram. (b)-(c): Reduced hologram δI (averaged over 9 exposures to enhance the display) and the modulus of $E_s^{(0)}(\bar{z}_A) = \hat{U}(\bar{z}_A - z_H) \left(\frac{\delta I}{E_r^*}\right)$ in \bar{z}_A plane. (d)-(e): Initial Gaussian beams profile in the $z = \bar{z}_A$ plane (plotted as $|E_G^{(0)}|$) and expected (reduced) hologram δI_e in $z = z_H$. The sub-figure on (e) is the residual $\delta I_e - \delta I$. (f)-(g): Modulus of the optimal Gaussian profiles $E_G = \langle E_s(\bar{z}_A) \rangle_G$ and the corresponding hologram. (h): Modulus of $\tilde{E}_s(\bar{z}_A)$ with Gaussian-approximated twin image removed. Eleven samples are labeled from left to right, from top to bottom. (i): Reconstructed OD, ϕ distributions. At $z = \bar{z}_A$, only the samples in dash-lined boxes are with the phase-shift ϕ rightly suppressed in-focus for $\Delta \ll \Gamma$.

pendix B 2 a) and phase-uniformity (Appendix B 2 c) constraints. With $n_A = 3$ Gaussians for each samples, the final Gaussian approximation $\langle E_s \rangle_G$ is displayed at $z = \bar{z}_A$ in Fig. 2f. The optimal δI_e is shown in Fig. 2g. Finally,

following Eq. (13), we obtain \tilde{E}_s which is displayed in Fig. 2h at $z = \bar{z}_A$.

With $\tilde{E}_s \approx E_s$ and E_r at hand, in Fig. 2i we evaluate φ_A for all the samples at the fixed, "common" $z = \bar{z}_A$, and plot the OD and ϕ images. The array of samples are axially displaced by tens of micrometers. Here, with $\Delta \ll \Gamma$ we expect $\phi \ll \text{OD}$ according to Eq. (18), which is satisfied for arrays of samples enclosed by dash-lined boxes only. For these samples, their z_A are close enough to \bar{z}_A in the display. For other samples, the out-of-focus images mixes OD with ϕ , as expected.

1. Sample position localization

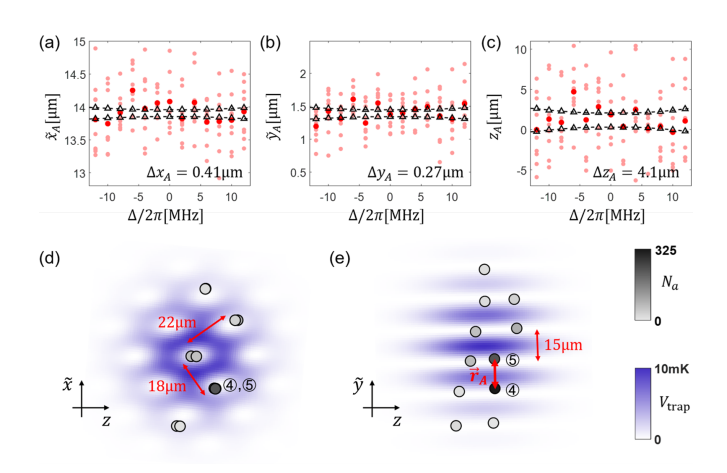


FIG. 3. (a)(b)(c): Relative displacement between two samples marked in (d)(e) (and Fig. 2h) estimated with single-shot δI using Eq. (B10) criterion. The single-shot estimation at different probe detunings are plotted with red dots. Black triangles indicate the photon-shot-noise limits according to Eq. (A10). The standard deviations Δx_A , Δy_A , Δz_A in the figures are averaged over all data at detunings between $-12 \mathrm{MHz} \leq \Delta/2\pi \leq 12 \mathrm{MHz}$. (d)(e): Visualization of the sample locations in the 3D lattice. Here the locations are collectively decided by the phase angles [19] using Eq. (18) with the $4 \mathrm{MHz} \leq |\Delta|/2\pi \leq 12 \mathrm{MHz}$ data. The atom number N_a is estimated by Eq. (18) with $\xi(s) \propto 1/(1+s)$ [72]. The circles represent the atomic samples with radius representing the sample sizes. The sizes are larger than Δx_A , Δy_A , as well as the collectively-improved $\Delta z_A \leq 1.5 \mu \mathrm{m}$.

With the E_s decomposition based on single-shot (I',I) data, we obtain a list of z_A and the low-resolution $\langle \varphi_A \rangle_G$ for each samples. Using $|\langle \varphi_A \rangle_G|$ in the x-y plane, the center-of-mass locations $\mathbf{r}_A = \{x_A, y_A, z_A\}$ are retrieved. As being outlined in Sec. II, for the $z_\sigma \ll z_A, z_H - z_A$ samples here, we refine the z_A estimation simply by reconstructing \tilde{E}_s with Eq. (13), and then re-applying the phase-angle uniformity criterion (Eq. (B10)). Depending on the E_s complexity and the n_A exploited for the decomposition ($n_A = 3$ here), the \tilde{E}_s -refinement generally leads to slightly improved z_A -estimation. Here, for samples with substantial OD and ϕ , such as the (4), (5) samples

ples for Fig. 2(a-c) data, this refinement corrects small Δ -dependent errors in z_A by 2 \sim 5 μ m.

To estimate the accuracy of the atomic sample localization, ideally we would like to analyze the fluctuation of the individual position values retrieved from repeated measurements. However, our sparse lattice is not stable enough. The lattice centers translate together by $1 \sim 2 \ \mu \text{m}$ from shot-to-shot, likely caused by pointinginstability of the lattice beams (Fig. 2a). While the fluctuation hardly impacts our axial, z_A -localization analysis, its suppression is required for analyzing the statistics on the more precisely located x_A, y_A values. To suppress the position fluctuation, in Fig. 3a-c we instead analyze the relative displacement between two samples. For the single-shot analysis we choose samples with largest atom numbers, marked as "4, 5" according to Fig. 2h. In Appendix A we evaluate the shot-noiselimited precision to $\Delta \mathbf{r}_A$ as the classical Cramer-Rao bounds with $N_s = \sum_{x,y} |E_{s,A}|^2$ photons (Eq. (A10)). We find the transverse $\Delta x_A, \Delta y_A$ are about a factor of $5\sim6$ larger than the 100 nm-level photon shot-noise limit (Eq. (A10)), which are likely due to shot-to-shot relative motion between the pair of samples. On the other hand, the 4 μ m axial Δz_A is a factor of 4 larger than the photon shot-noise limit (Eq. (A10)). That the single-shot Δz_A is quite far from the shot-noise-limit is likely related to non-optimal data analysis in presence of imaging noises. Nevertheless, both the transverse Δx_A , Δy_A , and the axial Δz_A , are already all well-below the diffraction limits set by $\lambda/NA = 3 \mu m$ and $2\lambda/NA^2 = 23 \mu m$, respectively.

Therefore, as in Fig. 3c, we are able to "super-resolve" z_A for each sample with $\sim 10^2$ atoms even using a singleshot (I', I)-data with $\tau_p = 20 \mu s$ exposure. The accuracy can be improved further by exploiting the spectroscopic constraint with the full $\{I', I\}$ data set [19] collectively. In particular, by enforcing the $\tan\beta \propto \Delta$ relation required by Eq. (18) for all the data (except for $|\Delta|/2\pi < 4$ MHz data, where the radiation pressure effect is most predominant, as following), our z_A estimation is substantially improved. For the (4), (5) samples, the Δz_A are reduced to below one micrometer. Comparing with single-shot z_A localization as in Fig. 3c, the refined z_A typically involves 2-3 μm additional corrections. These corrections helps to ensure that the samples are more consistently located within dark centers of the 3D lattice, as illustrated in Figs. 3(d)(e).

2. Complex-valued spectroscopic imaging

With the list of z_A and $\langle \varphi_A \rangle_G$ for each sample, we can proceed to evaluate $\tilde{E}_{s,A}$ with Eqs. (13)(16) and to approximately obtain φ_A with diffraction-limited resolution, according to Eq. (2). However, as discussed in Appendix A, the Eq. (9) shot-noise-limit to the phase-angle β is reached with fixed z_A . Without the knowledge, the phase-angle uncertainty $\Delta\beta$ is compromised by a factor of $1/\sqrt{2}$, at least. Therefore, we re-optimize

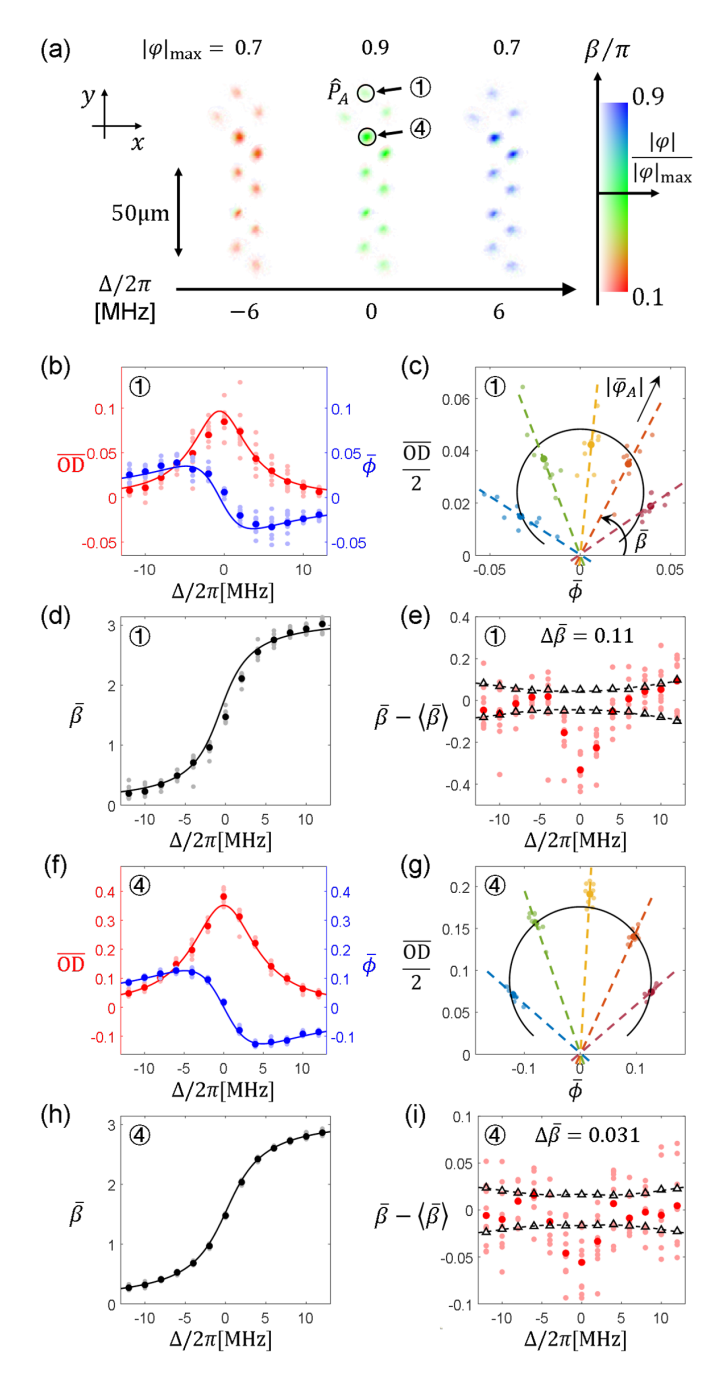


FIG. 4. Complex-valued spectroscopic imaging. (a): Color domain plot of φ_A with all the samples projected to the $z = \bar{z}_A$ plane. (b)(f): Average \overline{OD} , $\bar{\phi}$, within \hat{P}_A marked in (a), for "1,4" samples respectively. Solid (transparent) dots are average (individual) values of nine measurements. Solid lines are fitted according to Eq. (18). (d)(h): The phase-angle spectroscopy. Notice in (h) the 9 sets of data overlap closely. (c)(g): OD/2- ϕ phasor plot at $\Delta/2\pi$ = -6 MHz, -2 MHz, 0 MHz, 2 MHz and 6 MHz, in red, orange, yellow, green, and blue respectively. The black lines are according to the (b)(f) fits. (e)(i): Residuals of $\bar{\beta}$ from the (d,h) fits. Black triangles and dashed lines give photon-shot-noise limit [18] (Eq. (9)). The phase-angle uncertainty $\Delta \bar{\beta}$ of 0.11 and 0.031 are averaged over 4MHz $\leq |\Delta|/2\pi \leq 12$ MHz single shot data. The values are about a factor of two larger than the corresponding photon-shot-noise limit (Eq. (9)) [76].

the Gaussian decomposition, using the $\{I, I'\}$ -set, collectively improved z_A as prior knowledge. The phase-angle spectroscopy to be discussed in the following is based on such re-optimized single-shot Gaussian decomposition (Fig. 3(d,e)).

We now evaluate $\varphi_A = \varphi(z_A)$ using Eqs. (2)(16). The color-domain plots in Fig. 4a show φ_A , with phase angle β indicated by color and modulus $|\varphi_A|$ by brightness. In contrast to Fig. 2(i), $\varphi(z_A)$ s from various samples are "projected" to $z = \bar{z}_A$ from different z_A planes. In the plots we observe consistent phase-angle β at the same detunings Δ , as anticipated. It is also observed that the same sample may appear slightly different at various detunings. This slight distortion in shape is primarily attributed to the lensing effect as the probe passes through the microscopic samples.

To further demonstrate aspects of the complex-valued spectroscopy, in Figs. 4(b)(f) we choose $\widehat{1},\widehat{4}$ samples and plot $\widehat{OD} = 2\operatorname{Im}[\bar{\varphi}_A]$, $\bar{\phi} = \operatorname{Re}[\bar{\varphi}_A]$ as a function of the probe detuning Δ . Here $\bar{\varphi}_A$ is averaged over the sample area \hat{P}_A as suggested in Fig. 4a. The same data is further presented in Figs. 4(c)(g) as 2D phasor plots, and in Figs. 4(d)(h) in terms of phase-angle spectroscopy.

In Figs. 4(b)(f) we see data from the repeated single-shot measurements fluctuate substantially. A closer look suggests there are strong correlations between the $\overline{\text{OD}}$ and $\bar{\phi}$ fluctuations, which are more clearly seen in Figs. 4(c,g): The repeated measurements mostly spread the data points along the radial $|\varphi_A|$ direction instead of along β . These fluctuations are associated with the quite-expected atom number fluctuations in repeated measurements, which strongly affect the modulus $|\varphi_A|$ but hardly affect β , according to Eq. (18).

The β -stability is directly seen in the Fig. 4(d)(h) phase-angle plot. Here we use Eq. (18), with $\xi(s) \propto$ 1/(1+s), to fit the data. By excluding the -4 MHz < $\Delta/2\pi$ < 4 MHz data points from the fit, $s_0 \approx 1$ and $\Gamma \approx 6$ MHz can be extracted, agreeing excellently with expectation. The residuals are shown in Figs. 4(e)(i). Notably, for all the samples, we consistently see deviation of the β -data from the 2-level model within $\Delta < \Gamma/2$. As in Sec. IID, this deviation is caused by Doppler shifts associated with atomic motion. In particular, for the $\tau_p = 20 \ \mu \text{s}$ probe with $s_0 = 1$ on resonance, the atomic sample is expected to be accelerated to a final $v \approx 1 \text{ m/s}$ along \mathbf{e}_z . The average $k\overline{\Delta v}\sim 2\pi\times 640$ kHz Doppler shift is sensed by our complex spectroscopy, leading to $\delta\beta = 2k\Delta v/\Gamma \approx 0.2$ shift to the phase angle, according to Eq. (18). Remarkably, the shift is almost halved for the (4) sample, as in Fig. 4i, which is likely related to reduced radiation pressure [77] due to attenuation of the probe by the larger sample.

We note that on resonance the radiation pressure is also expected to displace the samples by up to 10 μ m along z. The average z_A displacement is $2 \sim 3 \mu$ m-level at most. The differential displacement between 4, 5 samples caused by the radiation pressure is below the axial resolution in Fig. 3(c).

We estimate the phase-angle resolution $\Delta\beta(\Delta)$ using the data statistics from Fig. 4(e)(i). Theoretically, for optically thin samples, the resolution $\Delta \bar{\beta}(\Delta)$ is constrained by $N_s(\Delta)$, which represents the number of coherently scattered photons E_s received by the camera, through the Eq. (9) relation (Appendix A). After applying a moderate correction for finite $|\varphi_A|$ as discussed in ref. [18], the shot-noise-limited $\Delta\beta$ values are evaluated according to Eq. (9) and marked with triangle symbols in Fig. 4(e)(i). We observe that the values of $\Delta \bar{\beta}$ closely follow the photon-shot-noise limit for both the (1) and (4) samples. By averaging the standard deviations of $\Delta \bar{\beta}(\Delta)$ across all data in Fig. 4, excluding the range $-4 \text{ MHz} < \Delta/2\pi < 4 \text{ MHz}$, we estimate statistically the single-shot resolution to be $\Delta \bar{\beta} \approx 0.11$ and 0.031 for the (1) and (4) samples, respectively [76]. For the (4) sample, the 30 mrad resolution in β suggests a frequency resolution of $\Delta\omega = 2\pi \times 100$ kHz, according to Fig. 4h and Eq. (18) near $\Delta = 0$, where $\Delta \omega = \Delta \beta \times \Gamma/2$ and $\Gamma = 2\pi \times 6 \text{MHz}.$

3. Field sensing

With the spectroscopic images of atomic arrays, it is possible to detect local perturbation to the $|g\rangle - |e\rangle$ transition frequency ω_{eg} in 3D with high spatial resolution. In this section, we demonstrate this field-sensing capacity by measuring the transition light shift induced by a "dressing" laser. The schematic setup is displayed in Fig. 5a. Right before the imaging exposure, a dressing laser E_m with a Gaussian radius of $w_m \approx 10~\mu\text{m}$, at $\lambda_m = 1064~\text{nm}$ and with power $P_m \approx 1~\text{W}$, is turned on. This leads to Stark shift $\delta\omega_{eg} \propto |E_m|^2$ of about 6 MHz. The shift is clearly seen in Fig. 5b with the φ_A images.

Taking a closer look at Fig. 5b, since the dressing beam is not uniform, the 3D-distributed samples experience slightly different $\delta\omega_{eg}$ shifts. In Fig. 5c we plot $\bar{\beta} = \arg(\bar{\varphi}_A)$ for three samples, labeled as (2), (4), (7) in Fig. 5b. For the convenience of display, we encode the sample index with the degree of transparency for the $\bar{\beta}$ curves. We clearly see that while in absence of dressing the β curves closely overlap (the red curves), the three $\bar{\beta}$ curves disperse apart when E_m is on (blue curves). The difference is most pronounced near the shifted ω_{eq} center, with $\Delta/2\pi \approx 6$ MHz, where β regains the highest Δ -sensitivity of $\partial_{\Delta}\beta \sim 2/\Gamma$ according to Eq. (18). By analyzing the spectra for all samples, we are able to resolve $\delta\omega_{eg}$ in 3D with micro-meter resolution. The spatialdependent light shift is most conveniently displayed in the x-z plane where the dressing beam is in focus. For the purpose, the vertical view of $\Delta\omega_{eq}$ is plotted in Fig. 5d for our eleven samples with significant $|\varphi_A|$.

The field-sensing capacity demonstrated in this section shares the same frequency resolution with that is discussed in the last section. In particular, according to Eq. (18) near the shifted ω_{eg} resonance, we again have $\Delta(\delta\omega_{eg})/2\pi \approx 100$ kHz. We emphasize this resolution is

achieved by $\sim 10^2$ atoms within $\tau_p = 20~\mu s$, with micronsized 3D resolution.

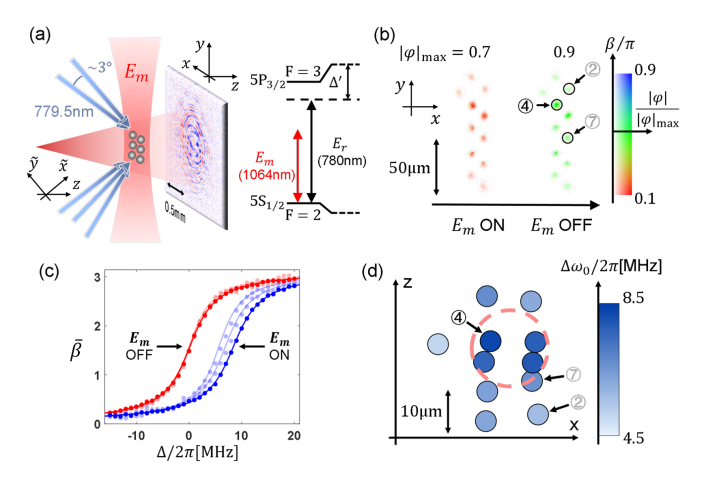


FIG. 5. Sensing light shifts with a sparse array of laser-cooled atoms. (a): Experimental setup and the level diagram. (b): \bar{z}_A -projected φ_A -images of the axially displaced samples, with and without E_m . The data are processed from δI averaged over 9 exposures to enhance the display. The probe detuning is $\Delta/2\pi=0$ MHz. (c): \hat{P}_A -averaged phase angle spectra of "2,4,7" samples marked in (b). The red (blue) curves are for E_m off (on). The transparency levels are according to the markers in (b). (d): x-z "top" view of the light shift distribution. The 11 largest- $|\varphi|$ samples are represented by blue disks. The dash-lined circle suggests the estimated E_m full-width-half-maximum focal spot in the x-z plane.

IV. DISCUSSIONS

A. Aberrations

So far, our holographic imaging scheme assumes aberration-free propagation of E_r , E_s between the sample plane z_A and hologram plane z_H . Practically, the $E_{r,s}$ wavefronts need to be optically relayed from the ultrahigh vacuum to the place where the digital camera sensor conveniently locates. For high-NA imaging, aberration becomes unavoidable when the required volume-of-view is large.

To describe the imperfect imaging, we consider both E_r and E_s as in Fig. 1a to be relayed from inside the ultrahigh vacuum where the actual light-atom interaction takes place. We use a wavefront propagator $U_{\rm img}$ to generally represent the linear transformation of wavefronts from the in-situ $z=z_{V,A}$ to $z=z_A$,

$$E_r(x, y, z_A) = U_{\text{img}} E_r(x_V, y_V, z_{V,A}),$$

$$E_s(x, y, z_A) = U_{\text{img}} E_s(x_V, y_V, z_{V,A}).$$
(19)

For imperfect imaging, the fundamental way to eliminate the associated imaging errors is to fully characterize the propagator $U_{\rm img}$. Then, by resolving $E_{r,s}(z_{V,A})$ through Eq. (19) to apply our prior knowledge about the

samples in situ. Practically, even with advanced computing power, the modeling of diffraction-limited E_r, E_s propagation across the large-diameter lens-array can still be prohibitively resource-demanding. On the other hand, the wavefront propagation is greatly simplified by Gaussian decomposition [32–34]. The well-developed technique is naturally adapted to the Gaussian-assisted holography scheme in this work to potentially enable aberration-free imaging of sparse samples over unprecedentedly large imaging volumes, only limited by the finest hologram fringes that can be captured by the camera [68].

To fully characterize $U_{\rm img}$ for the large-diameter lensarrays [73, 74], and to invert Eq. (19) with Gaussian-decomposition, are all beyond the scope of this work. Instead, we take advantage of the small volume-of-view (Fig. 2) to address minor, aplanatic aberrations. This is achieved by employing a point-spread function [43] O(x,y) through in situ optical measurements. The procedure is detailed in Appendix D 3.

B. Speckles

In addition to aberrations, the imaging optics may introduce speckle noise into the wavefronts through multiple reflections and even by small dusk particles on the optical surfaces. Since the probe beam for atomic spectroscopy is highly monochromatic, the speckle noises are difficult to avoid.

We denote δE_r and δE_s to be speckle fields generated by unwanted reflections and scatterings across the imaging optical path. We assume that the perturbations are static enough for their precise characterization through multiple measurements. With Gerchberg-Saxton iterations [18], δE_r is fully characterized in this work (Fig. 1b). When speckle noises in $E_{r,s}$ are moderate, as in this work, their presence hardly affect our prior knowledge about φ_A for the E_s retrieval (Sec. II). But the presence of δE_r does affect the φ_A retrieval with Eqs. (2), particularly since substantial amount of the speckle noises δE_r may be generated by imaging optics after the light-atom interaction, not "seen" by atoms at $z=z_A$. To minimize the δE_r impact, one should locate the sources of δE_r with digital propagation of E_r , and by removing the speckles to recover the actual E_r attending the light-atom interaction. The process of characterizing the speckle sources across the imaging path is therefore similar to characterizing $U_{\rm img}$ discussed above. If all the speckle scatterings in $\delta E_{r,s}$ are static enough, the procedure would help to fully suppress the associated noises in the φ_A retrieval.

In this work, we take a simpler approach to approximately suppress the speckle noise to the complex-valued spectroscopic imaging. In particular, during the Eq. (2) evaluation of φ_A , we simply filter away the apparent speckles from E_r . This is achieved by digitally focusing E_r back to z=0 and only choose a small region around the diffraction-limited component, before propa-

gating forward to $z=z_A$ for the φ_A evaluation. In other words, we assumes E_r "seen" by atoms is speckle-less, which is a good approximation in our setup, considering that comparing to the multiple-stage-relayed large-diameter imaging optics, the E_r is focused to atomic samples with simpler, smaller-diameter optics [73].

C. Summary

From precision spectroscopy [61, 62, 78] to quantum simulation [79], precise optical imaging [80–82] is crucially important for advancing ultracold atomic physics research at frontiers. The prevailing imaging method in these researches is to directly record fluorescence [80, 81, 83, 84], absorption [17, 85], and phase shift [20]. While holographic imaging techniques are rapidly developing for applications in other fields [59, 67, 86, 87], their utilities in atomic physics are rare [18, 30, 40–43]. In Sec. IB we highlighted major challenges of quantitative holographic imaging for precision spectroscopic measurements of cold atoms. In Sec. IC1 we provided arguments that the 3 dB information loss in holographic measurements hardly make them disadvantageous when comparing to direct imaging. If the challenges can be addressed, then, by extending the spectroscopy data to complex numbers and by enabling 3D resolution, the holographic method would help to unlock highly exciting opportunities associated with precise spectroscopic imaging and sensing on strong optical transitions.

In this work, motivated by the exciting prospect of complex-valued 3D spectroscopic imaging, we develop a systematic approach to address key challenges in holographic imaging of cold atoms (Sec. IB). Comparing with e.q. biological applications [46, 88], our choices of schemes and diversities in holographic measurements are severely constrained by aspects of cold-atom setups. Our philosophy is to fully characterize the imaging setup and to efficiently utilize all the available knowledge from single-shot inline holography. The efficient application of prior knowledge is numerically assisted by Gaussian beam propagation, a simple application of the well-established Gaussian-decomposition technique [32– 34, 89, 90. With the method, we have demonstrated complex-valued spectroscopic imaging of axially displaced microscopic ⁸⁷Rb samples in a sparse lattice, with micrometer 3D resolution. We achieve hundred-kHz-level single-shot frequency resolution out of the $\Gamma/2\pi = 6$ MHz natural linewidth, with merely hundreds of atoms, a result that appears extremely difficult to realize with traditional spectroscopy [1, 62], in presence of atom number and interaction strength uncertainties.

Not discussed in this paper is the observation of atomic shot noise [17, 43], which is barely supported by but nevertheless observed with our NA ≈ 0.26 setup. In addition, the imaging volume-of-view in this work is limited by the sample distribution itself to be within a $\sim 100~\mu \text{m}$ distance (Also see Appendix E). We clar-

ified in Sec. IV A that the technique can be extended to fully suppress wavefront aberrations for wide-field 3D imaging [91] of sparse atomic samples. The development may enable wideband, spectroscopic sensing of 3D potentials [15, 92] with unprecedented volume-of-view. Other than probing single-atom spectroscopic responses, our method also supports the study of resonant dipole interactions by simultaneously measuring the strength, direction and phase angle of the collective emission [25, 93]. As such, we also expect the complex-valued spectroscopic imaging method to facilitate efficient characterization and quantum engineering of advanced light-atom interfaces [78, 94–97].

ACKNOWLEDGEMENTS

We thank Professor Haidong Yuan for helpful discussions and suggestions. We acknowledge support from National Key Research Program of China under Grant No. 2022YFA1404204, from NSFC under Grant No. 12074083, and from the Original Research Initiative at Fudan University.

Appendix A: Cramer-Rao bounds to position and phase localization by inline holography

In this section, we consider the estimation of bulk properties of the atomic sample from the hologram I, I' specified in Eq. (3). The basic setup is illustrated in Fig. 1a. The bulk properties of interest include the 3D atomic central locations $\mathbf{r}_A = \{x_A, y_A, z_A\}$ and the total amplitude of the forward scattering E_s . To facilitate the derivations, we introduce five $\{\theta_j\} = \{x_A, y_A, z_A, \beta_{r,\text{off}}, \beta_{i,\text{off}}\}$ parameters. The last two parameters are the real and imaginary parts of an auxiliary complex phase offset in

$$\tilde{E}_s = e^{i\beta_{\text{off}}} \hat{U}(z_H - z_A) \left(E_r(z_A) (e^{i\varphi_A} - 1) \right). \tag{A1}$$

For example, with $|\varphi_A| \ll 1$, then $\beta_{r,\text{off}}$ offsets our estimation to phase-angle $\beta = \arg[\varphi_A]$, and $\beta_{i,\text{off}}$ offsets $|\varphi_A|$.

The hologram I is accordingly re-modeled as

$$\tilde{I} = \left| E_r(z_H) + \tilde{E}_s \right|^2 \tag{A2}$$

so that $I' = \tilde{I}|_{\beta_{\text{off}} \to 0}$. We regard $p(x,y) = \tilde{I}(x,y)/\sum_{x,y} \tilde{I}(x,y)$ as a 2D probability distribution of a single photon received by the camera. The Fisher information matrix is accordingly expressed as

$$F_{jk}^{(0)} \equiv \left(\sum_{x,y} \frac{1}{p(x,y)} \partial_{\theta_{j}} p(x,y) \partial_{\theta_{k}} p(x,y)\right)_{\beta_{\text{off}} \to 0},$$

$$\approx \left(\frac{\sum_{x,y} \frac{1}{\tilde{I}(x,y)} \partial_{\theta_{j}} \tilde{I}(x,y) \partial_{\theta_{k}} \tilde{I}(x,y)}{\sum_{x,y} \tilde{I}(x,y)}\right)_{\beta_{\text{off}} \to 0}.$$
(A3)

In the second line of Eq. (A3) we assumed the total flux $\sum_{x,y} \tilde{I}(x,y)$ received by the camera to be θ_j -independent, which is sufficiently satisfied for moderately-dense atomic samples in the defocused-twin regime (Appendix C1) with $z_\sigma \ll z_A, z_H - z_A$ (Fig. 1a), so that $|E_s| \ll |E_r|$ on the camera plane as to be assumed in the following. With $\partial_{\theta_j} \tilde{I} \partial_{\theta_k} \tilde{I} \approx |E_r|^2 (\partial_{\theta_j} \tilde{E}_s^* \partial_{\theta_k} \tilde{E}_s + c.c.) + (E_r^{*2} \partial_{\theta_j} \tilde{E}_s \partial_{\theta_k} \tilde{E}_s + c.c.)$, the second term also vanishes upon the 2D integration, due to the substantial wavefront mismatch between E_r and E_s . Equation (A3) is accordingly simplified into

$$F_{jk}^{(0)} \approx \frac{\sum_{x,y} \left(\partial_{\theta_j} \tilde{E}_s^* \partial_{\theta_k} \tilde{E}_s + c.c. \right)_{\beta_{\text{off}} \to 0}}{\sum_{x,y} |E_r|^2}.$$
 (A4)

The Fisher information matrix by Eq. (A4) is associated with single-photon detection on the camera. For imaging cold atoms, we are more interested in Fisher information associated with photons scattered by the samples [98]. A change of normalization leads to

$$F_{jk} = \left(\frac{\sum_{x,y} \partial_{\theta_j} \tilde{E}_s^* \partial_{\theta_k} \tilde{E}_s + c.c.}{\sum_{x,y} |\tilde{E}_s|^2}\right)_{\beta_{\text{off}} \to 0}.$$
 (A5)

Interestingly, Eq. (A5) suggests Fisher information for holographic measurements upon a single E_s -photon detection is equal to half of the quantum Fisher information [35] for the E_s -photon wavepacket. This 50% loss of information is generally associated with heterodying measurements [30].

From a single photon wavepacket to $N_s = \sum_{x,y} |E_s|^2$ photons detected by the camera in an uncorrelated manner, we have $F_{jk}(N_s) = N_s F_{jk}$ according to Eq. (A5) to limit the resolutions of $\{\theta_j\}$ measurements with the associated Cramer-Rao bounds. With Eq. (A1), evaluation of Eq. (A5) for the $\beta_{r,\text{off}}$, $\beta_{i,\text{off}}$ differentiation is straightforward. With the free-space propagator $\hat{U}(z_H - z_A)$ by Eq. (D1) to be x_A, y_A independent, the translational invariance suggests

$$\partial_{x_A} \tilde{E}_s = -\partial_x \tilde{E}_s,
\partial_{u_A} \tilde{E}_s = -\partial_u \tilde{E}_s.$$
(A6)

For the differentiation of the z_A -parameter in Eq. (A5), we rewrite

$$\tilde{E}_s = e^{i\beta_{\text{off}}} \hat{U}(z_H - z_A) \left(\left(\hat{U}(z_A) E_r(0) \right) \left(e^{i\varphi_A} - 1 \right) \right). \tag{A7}$$

Here the first propagator $\hat{U}(z_H - z_A)$ acts on $E_s(z_A) = E_r(z_A)(e^{i\varphi_A} - 1)$. The second $\hat{U}(z_A)$ acts on $E_r(0)$ only. In the $z_\sigma \ll z_A$ (Fig. 1a) limit, the $E_r(z_A)$ "seen" by the σ -sized atomic sample can be approximated by plane wave. For on-axis samples we therefore find

$$\partial_{z_A}\tilde{E}_s \approx i(-\sqrt{k_0^2 + \partial_x^2 + \partial_y^2} + k_0)\tilde{E}_s.$$
 (A8)

With Eqs. (A1)(A6)(A8), evaluation of Eq. (A5) becomes straightforward for specific imaging setup, E_r -illumination, and atomic samples. To provide the Cramer-Rao bounds with a simple example, in the following we consider E_r to propagate along the z-axis, $E_s(z_A)$ to be the forward scattering by a Gaussian shaped sample located on the z-axis with a density distribution of $\rho_c = \rho_0 e^{-(x^2+y^2)/\sigma^2}$. We assume $\varphi_A = k_0 \rho_c \alpha(\omega) \ll 1$ so that the E_s amplitude simply follows the ρ_c profile, while $\sigma > \lambda/\text{NA}$ so that E_s is almost fully captured by the camera. By normalizing x_A, y_A with σ , and z_A with z_σ , the rescaled Fisher information matrix with N_s scattered-photon detection is

$$F(N_s) = N_s \begin{bmatrix} 2 & 0 & 0 & 0 & 0 \\ 0 & 2 & 0 & 0 & 0 \\ 0 & 0 & 1 & 1 & 0 \\ 0 & 0 & 1 & 2 & 0 \\ 0 & 0 & 0 & 0 & 2 \end{bmatrix}.$$
 (A9)

Clearly, while x_A, y_A and $\beta_{i,\text{off}}$ measurements are independent, the axial position z_A is correlated with the phase angle $\beta_{r,\text{off}}$. By diagonalizing Eq. (A9) and evaluate the Cramer-Rao bounds indirectly using the eigenvector observables, one finds that in the $\varphi_A \ll 1$ optically-thin-sample limit,

$$\Delta x_A = \sigma / \sqrt{2N_s},$$

$$\Delta y_A = \sigma / \sqrt{2N_s},$$

$$\Delta z_A = z_\sigma / \sqrt{N_s/2},$$

$$\Delta \beta = 1 / \sqrt{N_s},$$

$$\Delta |\varphi_A| = 1 / \sqrt{2N_s}.$$
(A10)

The axial resolution Δz_A can be enhanced to $\Delta z_A = z_\sigma/\sqrt{N_s}$ limit (Eq. (8)) [19] by taking multiple spectroscopic measurements to fix β first. On the other hand, with the axial position z_A fixed, the phase angle resolution for the sample is enhanced to $\Delta\beta = 1/\sqrt{2N_s}$ (Eq. (9)) [18].

Appendix B: Details of Gaussian decomposition

1. Gaussian beam

Gaussian decomposition is associated with a class of powerful semi-classical wave-propagation techniques [32–34, 89, 90]. We focus on the free Gaussian-propagation to support evaluation of E_r , E_s across z-planes during the minimization of \mathcal{L}_{tot} in Eq. (10).

The standard form of a Gaussian beam is expressed as

$$G_z(\mathbf{r}; \mathbf{P}') = e^{i(\mathbf{r}_{\perp} - \mathbf{r}_{\perp}^0)^T \frac{k_0}{2\mathbf{q}(z)}(\mathbf{r}_{\perp} - \mathbf{r}_{\perp}^0) + ik_0z + i\varphi_G(z)}.$$
 (B1)

Here $\mathbf{r}_{\perp} = (x, y)^T$. The complex $\mathbf{q}(z)$ -parameter is defined by

$$\frac{1}{\mathbf{q}(z)} = \begin{bmatrix} \frac{1}{R_x} + i\frac{2}{k_0 w_x^2} & 0\\ 0 & \frac{1}{R_y} + i\frac{2}{k_0 w_y^2}, \end{bmatrix}.$$
 (B2)

with

$$w_c(z) = w_c^0 \sqrt{1 + \frac{(z - z_c^0)^2}{(z_c^R)^2}},$$

$$R_c(z) = z - z_c^0 + \frac{(z_c^R)^2}{z - z_c^0},$$
(B3)

all decided by the Gaussian waists w_c^0 for c = x, y. The Gouy phase $\varphi_G(z)$ is given by

$$\varphi_G(z) = \frac{1}{2} \sum_{c=x,y} \arctan((z - z_c^0)/z_c^R).$$
 (B4)

The Rayleigh lengths are defined as

$$z_c^{\rm R} = \pi(w_c^0)^2 / \lambda \tag{B5}$$

for c = x, y.

Next, we introduce a rotation matrix $\mathcal{R}(\gamma)$ with Euler angles $\gamma = (\theta_1, \theta_2, \theta_3)$, so that $\mathbf{k} = (0, 0, k_0)\mathcal{R}(\gamma)$ is expressed as

$$\mathbf{k} = (-\sin\theta_2, \sin\theta_1 \cos\theta_2, \cos\theta_1 \cos\theta_2)k_0. \tag{B6}$$

The rotation angle θ_3 orients the principal axis of the 2D Gaussian profile. With $\mathbf{r} = (x, y, z)^T$, we have

$$G(\mathbf{r}; \mathbf{P}) = G_z(\mathcal{R}^T(\gamma)\mathbf{r}; \mathbf{P}').$$
 (B7)

Overall, with $\mathbf{P} = \{\gamma, \mathbf{P}'\}$, there are a total number of nine parameters $\mathbf{P} = \{\theta_1, \theta_2, \theta_3, x^0, y^0, z_x^0, z_y^0, w_x^0, w_y^0\}$ for a 2D Gaussian beam. To decompose a wavefront into n_A beams as in Eq. (7) involves a total number of $11 \times n_A$ real parameters $\{c_j, \mathbf{P}_j\}$.

2. Implementing the sample constraints

For a single sample as in Fig. 1 as well as multiple samples, our prior knowledge about the sample can often be formulated into a list of cost-functions C_{μ} to constrain the expected 2D complex-valued phase shift distribution, $\varphi(z_A) = \varphi_A$. The constraints help to fix the phase-ambiguity associated with $E_{s,\text{twin}}$ while locating the sample planes at $z=z_A$. In the following we provide examples of such C_{μ} -constraints, generalized for multiple samples.

a. Finite spatial support

The prior knowledge on the regime of interest where the atomic samples should be constrained within, as schematically illustrated in Fig. 1c with \hat{P}_A , is a condition commonly applied for coherent imaging [29, 30, 58, 99]. Here, for multiple atomic samples, the constraint can be formulated as a request to minimize the cost function,

$$C_{\mu} = \sum_{A} \frac{1}{\mathcal{N}_A} \sum_{x,y} |\varphi(z_A) - \hat{P}_A(\varphi(z_A))|^2.$$
 (B8)

Here $\mathcal{N}_A = \sum_{x,y} |\hat{P}_A(\varphi(z_A))|^2$ normalizes the error signal from each sample at the respective $z = z_A$.

b. Known phase angle

As being outlined in Sec. I and discussed in Sec. II D, for complex-valued atomic spectroscopy of a dilute gas, the phase angle $\beta = \arg(\varphi_A)$ is often decided by the polarizability of single constituent atoms, $\beta_0 = \arg(\alpha)$, and is therefore precisely known. The knowledge can be applied to constrain the $\langle E_s \rangle_G$ -search by minimizing

$$C_{\mu} = \sum_{A} \frac{1}{\mathcal{N}_{A}} \hat{P}_{A} \sum_{x,y} \left| \operatorname{Im}[\varphi(z_{A}) e^{-i\beta_{0}}] \right|^{2}.$$
 (B9)

That is, by unwrapping the known phase angle β_0 from the complex-valued phase shift, $\varphi_A e^{-i\beta_0}$ should be real, with vanishing imaginary component across each sample.

The Eq. (B9)-minimization is a generalization to previous phase angle constraints in holographic microscopy, such as positive attenuation criterion [60] and phase object criterion [42]. Application of Eq. (B9) requires the phase angle $\beta = \beta_0$ as precise prior knowledge. Practically, β_0 can be obtained by pre-characterization of standard samples first [19]. In particular, for free atoms, $\beta_0(\Delta)$ can be fixed by exploiting the Eq. (18) relation across the atomic resonance under study first (during which the axial location z_A for the standard samples are fixed too, as in Sec. III B 1).

c. Phase-angle uniformity

Without the precise β_0 knowledge, one still can exploit prior knowledge on β in holography. A common situation is that the atomic sample is monomorphous [41], with a uniform albeit not-precisely-known $\beta = \arg(\varphi_A)$ across the sample. The condition can be formulated as to minimize

$$C_{\mu} = \sum_{A} \frac{1}{\mathcal{N}_{A}} \hat{P}_{A} \left(\left| \sum_{x,y} \varphi(z_{A}) \right| - \sum_{x,y} \left| \varphi(z_{A}) \right| \right)^{2}.$$
 (B10)

d. Other types of constraints

Beyond the simple examples by Eqs. (B8)(B9)(B10), more sophisticated form of prior knowledge about the samples can be applied to tailor the cost functions $C_{\mu}(\varphi)$. For example, the finite support in Eq. (B8) can be replaced by a continuously varying \hat{P}_A according to our expectation of the sample shape. Similar strategies can be applied to soften the β_0 bounds in Eq. (B9) [60]. Other cost functions may be tailored to encourage the $\varphi(z_A)$ distribution meeting our expectation of a mixed spatial-spectral characteristics, such as for atomic samples confined by a dipole trap [100].

3. Direct constraints

a. Direct constraints to Gaussian parameters

Instead of formulating C_{μ} cost functions, simple knowledge about the sample can also be applied as direct constraints to the Gaussian parameters. For example, the finite spatial support in Eq. (B8) can be effectively enforced by limiting the range of \mathbf{r}_A and $w_x(z_A), w_y(z_A)$ parameters (Eq. (B7)). As another example, in the $|\varphi(z_A)| \ll 1$ weak scattering limit the phase-angle relation by Eq. (B10) effectively enforce the wavefront radii of curvature $R_x(z_A), R_y(z_A)$ to follow the $\langle E_r \rangle_G$ values.

b. Wavefront templates

Direct constraints to groups of Gaussian parameters become particularly useful when the E_s is expected to be characterized by certain wavefront template. Examples include synthesizing the point-spread-functions of high-NA microscopes [101], or for finely matching the expected shape of an interacting degenerate gas [102]. To form the template, the Gaussian-decomposition of the wavefront template is generally expressed as

$$\tilde{G}_{\text{template}}(\mathbf{r}) = \sum_{g} c_g G(\mathbf{r}; \mathbf{P}_g).$$
 (B11)

The $\tilde{G}_{\text{template}}$ with correlated Gaussian parameters $\{c_g, \mathbf{P}_g\}$ then enters the \mathcal{L}_{tot} -minimization, together with other individual Gaussian beams if necessary.

c. Beyond paraxial

Finally, the Gaussian propagation by Eq. (B2) is based on paraxial approximation which limits the propagation distance L to $L \ll (z_c^R)^2/\lambda$. To enhance the distance of faithful propagation, any Gaussian beam that is tightly focused around $z = z_A$ can be expanded into a superposition of weakly focused Gaussians according to Eqs. (B7)(B11).

Appendix C: Out-of-focus effects

1. Defocused-twin regime

In the Fig. 1a inline setup with the spherical E_r illumination, the twin-image $E_{s,\text{twin}}$ (Eq. (5)) is paraxially focused to $z=z_{\text{twin}}$. With $z_{\sigma} \ll z_A, z_H-z_A$, the $E_{s,\text{twin}}$ is sufficiently defocused at $z=z_A$. In absence of imaging noise, isolation of E_s from $E_{s,\text{twin}}$ becomes possible by limiting the E_s location \hat{P}_A with tight enough size of order σ [58]. We refer this inline holography regime that supports simple twin-image removal as "defocused-twin

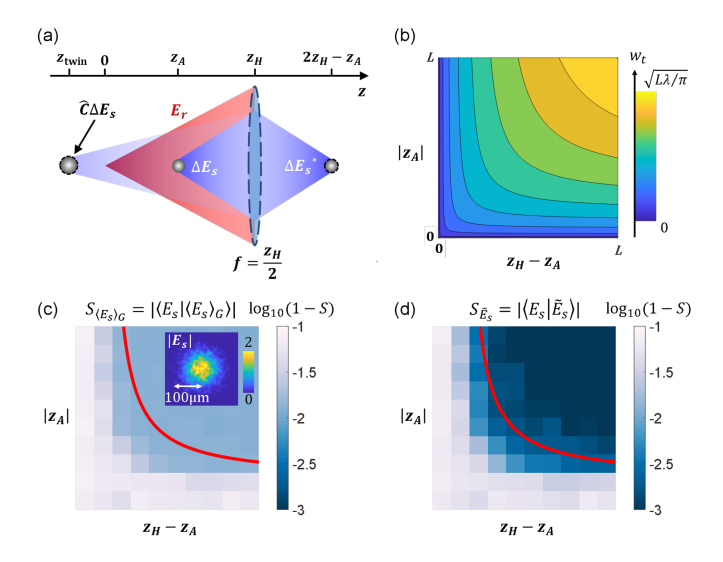


FIG. 6. (a): Schematic diagram of the geometric relation between image and twin image when $z_A < z_H/2$. The ΔE_s^* is a mirror-image of ΔE_s at the other side of the holographic plane z_H . For spherical E_r , the E_r/E_r^* term acts as a numerical lens with a focal length $f=z_H/2$. (b): The critical Gaussian beam size w_t as a function of z_A and z_H-z_A . (c): Fidelity of reconstructing E_s using the Gaussian E_G (Eq. (7)) approximations (Eq. (C5)). Here the simulated E_s follows a Gaussian profile with pixel-wise, Poissoinian atomic shot noise. The atom number is set to be 3500 in the simulation. The plot is averaged over $16 E_s$ simulations. The red line sets the critical Gaussian w_t . A typical numerically generated E_s from such a sample is given in the inset. (d): Fidelity plot similar to (c) but with $\langle E_s \rangle_G$ replaced by \tilde{E}_s (Eq. (16)) to substantially improve the accuracy.

regime". In the following we exploit Gaussian optics to derive a characteristic Gaussian width w_t , as a function of z_A and $z_H - z_A$, that sets the boundary of this regime for imaging small samples.

We consider that in the Fig. 1a setup the numerical reconstruction of certain E_s is contaminated by an error term ΔE_s , which is itself a Gaussian beam with complex radius of curvature $q=\frac{1}{a+ib}$ at $z=z_A$. Within the paraxial approximation, the twin image, expressed as $\Delta E_{s,\text{twin}}=\Delta E_s^*E_r/E_r^*$ at the camera plane $z=z_H$, is also a Gaussian. We evaluate the twin profile $\Delta E_{s,\text{twin}}$ at $z=z_A$ in four steps: propagation ΔE_s to z_H plane; taking the complex conjugation; passing through an ideal thin lens with a focal length of $z_H/2$; and propagating to $z=z_A$ plane. The complex curvature of the $\Delta E_{s,\text{twin}}$ at $z=z_A$ is given by:

$$q_{\text{twin}} = \frac{q(2z_A - z_H) + 2z_A(z_H - z_A)}{2z_A - z_H - 2q}$$
 (C1)

Now, if $|\Delta E_s| \ll |E_r|$, then it is easy to show that the artifact field $E_{\rm arti} = (\Delta E_s - \Delta E_s^* E_r / E_r^*)$ can be added freely to E_s without affecting the expected hologram $I_e = |E_r + E_s|^2$. In other words, if the hologram data (I, I') and E_r are all the prior knowledge we have, then the $E_{\rm arti}$ term is free to contaminate E_s during its recontaminate

struction. However, if \hat{P}_A has a width that is smaller than the smallest possible $E_{\rm arti}(z_A)$, then all the artifacts $E_{\rm arti}$ can be excluded. Here, the minimal width of $E_{\rm arti}(z_A)$ associated with the Gaussian ΔE_s and $\Delta E_{s,\rm twin}$ is set by equating their widths at $z=z_A$, that is, by equating the imaginary parts of 1/q and $1/q_{\rm twin}$. We obtain

$$b^{2} = -a^{2} - \frac{2z_{A} - z_{H}}{z_{A}(z_{H} - z_{A})}a + \frac{1}{z_{A}(z_{H} - z_{A})}.$$
 (C2)

Next, by maximizing b^2 (see Eq. (B2)), we obtain the minimal $E_{\rm arti}$ width

$$w_t = \sqrt{\frac{2\lambda z_A(z_H - z_A)}{\pi z_H}}. (C3)$$

Typical w_t according to Eq. (C3) is given in Fig. 6b. With Eq. (C3), the defocused-twin condition $z_{\sigma} \ll$ $z_A, z_H - z_A$ is also expressed as $\sigma \ll w_t$. With $\sigma = \eta w_t$ and $\eta \ll 1$, the hologram δI contains sufficient information to recover the Gaussian shaped E_s without requiring additional prior knowledge. Furthermore, by converting $\langle E_s \rangle_G$ into its twin, $\langle E_{s,\text{twin}} \rangle_G = \left(\frac{E_r}{E_r^*} \langle E_s \rangle_G^*\right)_{z=z_H}$, its contribution to δI is subtracted away as in Eq. (13). The high-spatial-frequency twin-image residual spreads out at $z = z_A$ with a width that is at least w_t/η . Its impact to E_s is therefore limited by $R\eta^2$ at least. Here $R \ll 1$ is the fractional residual of the Gaussian fit to E_s . As in the Fig. 6d example, for small enough samples (e.g., $\eta \sim 0.3$) with good Gaussian-fits (e.g., R < 0.1), the Eq. (16) approximation to E_s can be highly accurate. From Eq. (C3), it is also clear that for a fixed z_H distance between the point source and the camera plane, w_t reaches its maximum $\sqrt{\frac{\lambda z_H}{2\pi}}$ at $z_A = z_H/2$. In other

2. Overlapping samples

words, for inline-holographic imaging of large samples

under spherical wave illumination, one prefers to set

 $z_A \approx z_H/2$ to maximize the recordable E_r , E_s wavefront

mismatch for the efficient twin-removal.

In Sec. II, our discussions of Gaussian-assisted holographic imaging exploit a single-sample example as illustrated in Fig. 1a. The procedure is then generalized in a straightforward manner to non-overlapping samples weakly displaced along z. Here, we more generally consider 3D distribution of samples. A necessary condition to separate $E_{s,A}$ from each sample is that the wavefronts from any two samples are orthogonal to each other,

$$\langle E_{s,A}|E_{s,A'}\rangle = 0. \tag{C4}$$

Here the wavefront inner product is defined as

$$\langle E_a | E_b \rangle \equiv \frac{\int \mathrm{d}x \mathrm{d}y E_a^* E_b}{\sqrt{(\int \mathrm{d}x \mathrm{d}y | E_a|^2)(\int \mathrm{d}x \mathrm{d}y | E_b|^2)}}.$$
 (C5)

It is easy to show that the inner product is invariant along z, and can therefore be evaluated at any z-plane. For the weakly displaced samples considered in Sec. II with $\Delta z_{A,A'} \ll z_{\sigma}, z_{\sigma'}$, the Eq. (C4) orthogonality is guaranteed by non-overlapping samples within $z=z_A,\ i.e.,$ $\sqrt{\Delta x_{A,A'}^2 + \Delta y_{A,A'}^2} \gg \sigma + \sigma'$. Here σ, σ' are the characteristic widths of the samples at $z=z_A,z_{A'}$ respectively.

On the other hand, when $E_{s,A}$, $E_{s,A'}$ have substantial overlap at either $z=z_A$ or $z=z_{A'}$, then the relative axial displacement must be large enough, $\Delta z_{A,A'}\gg z_\sigma+z_{\sigma'}$, to guarantee the wavefront orthogonality.

With Eq. (C4) and given sufficient additional prior knowledge about the samples, the Gaussian-decomposition of E_s prescribed in Sec. II can be proceeded to obtain $\langle E_s \rangle_G = \sum_A \langle E_{s,A} \rangle_G$. Then, to approximately retrieve diffraction-limited $E_{s,A}$ using \tilde{E}_s from Eq. (13), Eq. (16) is modified as

$$\tilde{E}_{s,A} = \tilde{E}_s - \sum_{A' \neq A} \langle E_{s,A'} \rangle_G,
E_{s,A}(z_A) \approx \hat{P}_A(\tilde{E}_{s,A}(z_A)).$$
(C6)

Finally, Eq. (C6) can be iteratively refined, with the \hat{P}_A support, by replacing the $\sum_{A'\neq A} \langle E_{s,A'} \rangle_G$ term in the first line with the resulting second line.

Appendix D: Details of numerical implementation

1. Free propagation

In the Fig. 1a setup, we assume the wavefronts propagate freely for z>0. The propagation operator $\hat{U}(\Delta z)$ is conveniently written in the angular spectrum basis as

$$\hat{U}(\Delta z) = \mathcal{F}^{-1} e^{i\sqrt{k_0^2 - k_x^2 - k_y^2} \Delta z} \mathcal{F}.$$
 (D1)

Here $\mathcal{F} = \mathcal{F}_{x,y}^{k_x,k_y}$ represents 2D Fourier transformation such that $E(k_x,k_y,z) = \mathcal{F}_{x,y}^{k_x,k_y}(E(x,y,z))$.

The free-space propagator is applied to retrieve

The free-space propagator is applied to retrieve $E_r^{(0)}$ [18], as well as to obtain $E_s(z_A)$ with Eq. (13) during the final step of $\varphi(z_A)$ reconstruction.

2. Nonlinear optimization

We follow an adaptive moment estimation algorithm [103] to minimize Eq. (10) in small steps. Taking advantage of the analytical Gaussian expression by Eq. (B7), we randomly sample a small fraction of x, y pixels in δI during the evaluation of \mathcal{L}_H . We find in most cases, the sparse sampling of about 1% of full data is sufficient to ensure the convergence of the nonlinear optimization. Similarly, during the evaluation of \mathcal{L}_A associated with e.g. Eqs. (B8)(B9)(B10), we find that by evaluating 5% of pixels within \hat{P}_A is sufficient to ensure the convergence.

To analyze a set of holograms from similar experimental measurements, the very initial guess of Gaussian parameters are obtained by fitting the Eq. (13) approximation to $E_s(z_A)$ but with $\langle E_s \rangle_G$ set to zero (the $E_s^{(0)}(\bar{z}_A)$ in Fig. 2b). Following the optimization for the first measurement, the optimal z_A , $\{c_j, \mathbf{P}_j\}$ parameters are transferred to initialize the optimization in similar measurements. Here, it is worth noting that while the parameter transfer greatly speed up the nonlinear optimization, the method is prone to cumulative numerical errors if the nonlinear optimization does not fully converge. To verify that the results are free from the accumulative errors, we often deliberately reset a set of parameters to far-fromoptimal values during the parameter transfer.

3. Aberration corrections

Following Eq. (19) and for the convenience of presentation, we define the "ground-truth" fields $E_{r,s}^{(0)}(x,y,z_A) = E_{r,s}(Mx_V,My_V,z_{V,A})$ between a specific pair of $z_A,z_{V,A}$ planes, with M to be the magnification factor. With $U_{0,\rm img}$ to represent the perfect wavefront transformation, we have

$$E_r(z_A) = U_{\text{img}} U_{0,\text{img}}^{-1} E_r^{(0)}(z_A),$$

$$E_s(z_A) = U_{\text{img}} U_{0,\text{img}}^{-1} E_s^{(0)}(z_A).$$
 (D2)

The key insight about aplanatic aberration correction is that for $E^{(0)}(x_0, y_0, z_A)$ within a small enough imaging area at the z_A -plane,

$$E(x, y, z_A) = \int dx_0 dy_0 E^{(0)}(x_0, y_0, z_A) O(x - x_0, y - y_0).$$
(D3)

Here O(x, y) is the complex point-spread-function of our imaging system around $\mathbf{r}_A = (x_A, y_A, z_A)$.

Experimentally, we obtain O(x,y) by directly measuring E'_r , the probe beam E_r (Fig. 1a) with its focus translated to the sample location \mathbf{r}_A . Similar to the E_r -phase recovery in Fig. 1b, we take intensity profiles of E'_r at multiple planes to reconstruct the complex E'_r -profile, using the Gerchberg-Saxton iterations [18]. By assuming E'_r to be diffraction-limited itself, we obtain the complex point-spread function as $O(x,y) = E'_r/|E'_r|_{\text{max}}$, up to the NA=0.3 numerical aperture [73]. Notice here O(x,y) at $z=z_A$ can be propagated to other z-planes through Eq. (D1), such as to obtain $O(x,y,z_H)$ at the $z=z_H$ camera plane to correct for the wavefronts there, as long as those wavefronts can be back-focused around \mathbf{r}_A .

With O(x, y) at hand, we exploit Eq. (D3) in two ways. First, during Gaussian decomposition of E_s for atomic sample centered at x_A, y_A , in particular for the evaluation of Eq. (11), we simply multiply $O(x-x_A, y-y_A, z_H)$ to the associated E_G . In other words, at this stage we approximate the Gaussians profiles as 2-dimensional δ -functions at $z=z_A$ and directly exploit Eq.(D3) to estimate the aberrated Gaussians at the camera plane.

Second, during the final evaluation of E_s (Eq. (16)) and E_r (Eq. (17)), we divide E_s and a windowed E_r by $O(k_x, k_y)$ in k-space. Here E_r is selected to within an area-of-interest, with a size close to the Fig. 2 display. To minimize edge effects, a Blackman-window is applied for the E_r selection.

Finally, we note that in our imaging system with $M \neq 1$, the simple volumetric data process is subjected to the paraxial approximation, *i.e.*, by Taylor-expanding the $k_{x,y}$ -dependent phase shift in Eq.(D1) to the second order only. This paraxial condition is well-satisfied in the experimental demonstration where the axial displacements of samples are moderate (Fig. 2).

Appendix E: Imaging larger samples

The experimental work presented in Sec. III exploits small atomic samples distributed in 3D. Due to their regular shapes, a total number of $n_A = 3$ Gaussians suffices the decomposition of $E_{s,A}$ for each sample. In this section, we provide an example of imaging larger, more complex samples.

As in Fig. 7a, the cigar-shaped sample is released from the 1064 nm dipole trap (which acts as the E_m -field in the Fig. 5 measurement). During the $\tau_p = 20 \ \mu s$ imaging exposure, a "dimple trap" beam \vec{E}_d at 840 nm is switched on to dress the atoms with its $w \approx 10 \ \mu \text{m}$ focal spot. Similar to the Sec. III experiment, we repeat the atomic sample preparation to take the $\{I, I'\}$ dataset with $\Delta/2\pi$ scanned between -18 MHz and +18 MHz. Part of the data are presented in Fig. 7. The OD-image in Fig. 7b and the (Δ', ρ_c) - images in Fig. 7c are all derived from the complex φ_A -data reconstructed from "singleshot" δI , as following. Similar to Fig. 2, here each δI is also averaged over nine repetitions to enhance the display. We follow the Sec. II prescription with $n_A = 16$ for the Gaussian decomposition of E_s . There are eight Gaussians to capture the global cigar shape, and another eight Gaussians to capture the local structure around the dimple-dressing beam. We then obtain \tilde{E}_s according to Eq. (13) and approximated φ_A according to Eq. (16). In Fig. 7c at different probe detuning Δ , we consistently see the local Stark-shift spot with $\delta\omega_{eq}\approx 2\pi\times 4$ MHz.

Similar to Fig. 4, we average the φ_A -data (not shown) over two circular Region-Of-Interest(ROI), suggested in the Fig. 7c (Δ' , ρ_c) plot, to compile $\overline{\text{OD}}$, $\bar{\phi}$ in Fig. 7(d) and $\bar{\beta}$ data in Fig. 7(e). By fitting Fig. 7(d,e) spectroscopy data for free-flying atoms with Eq. (18), the probe intensity parameter $s_0 \approx 1.2$ and the transition linewidth $\Gamma = 2\pi \times 6.0$ MHz are extracted, which are

highly agreeable to expectations. For the Fig. 7c (Δ', ρ_c) -images, the local detuning $\Delta' = -\frac{\Gamma}{2} \tan \beta$ is derived from $\beta = \arg[\varphi_A]$ similar to Fig. 4. The atomic column density ρ_c is estimated with Eq. (18) with $\xi(s) = C^2/(1+s)$ [72].

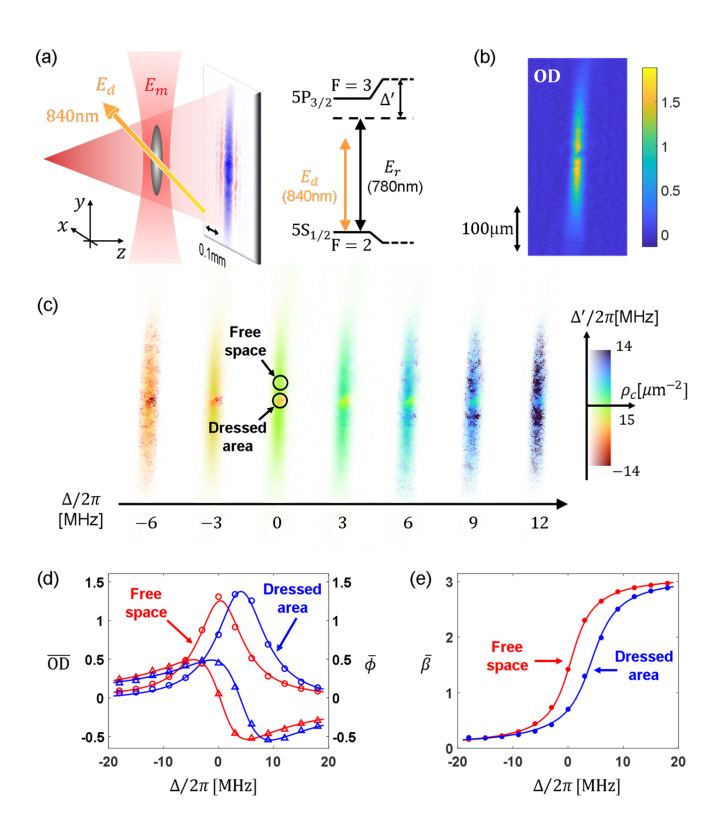


FIG. 7. Spectroscopic imaging of a cigar-shaped atomic sample, released from a dipole trap (E_m) , and subjected to a "dimple" E_d dressing. (a): The Experimental setup and the level diagram. (b): Typical optical depth image, processed from δI averaged over 9 exposures to enhance the display. Here the probe detuning is $\Delta/2\pi = 0$ MHz. (c): (Δ', ρ_c) in color domain plots. Here ρ_c is column density, and $\Delta' = -\frac{\Gamma}{2} \tan \beta$ is the local detuning, both derived from the complex φ_A -data similar to Fig. 4a. (d): ROI— averaged $\overline{\rm OD}$ and $\overline{\phi}$ spectroscopy. The two Region-Of-Interest (ROI) are marked in (c). The red (blue) curves correspond to region without (with) the E_d -dressing. The solid lines are according to Eq. (18) with $\xi(s) \propto 1/(1+s)$. (e): The phase-angle spectroscopy of the same data. Similar to Fig. 4(b-i), the fits for the free-space data here give $s_0 = 1.2$ and $\Gamma = 2\pi \times 6.0$ MHz, within expectations.

C. J. Sansonetti, C. E. Simien, J. D. Gillaspy, J. N. Tan, S. M. Brewer, R. C. Brown, S. Wu, and J. V. Porto, Absolute transition frequencies and quantum interference

in a frequency comb based measurement of the Li6,7 D lines, Physical Review Letters 107, 023001 (2011).

^[2] Z. Lu, P. Mueller, G. W. F. Drake, and S. C. Pieper,

- Colloquium: Laser probing of neutron-rich nuclei in light atoms, Rev. Mod. Phys. 85, 1383 (2013).
- [3] A. Beyer, L. Maisenbacher, A. Matveev, R. Pohl, K. Khabarova, A. Grinin, T. Lamour, D. C. Yost, T. W. Hänsch, N. Kolachevsky, and T. Udem, *The Rydberg constant and proton size from atomic hydrogen*, Science 358, 79–85 (2017).
- [4] S. Fuchs, R. Bennett, R. V. Krems, and S. Y. Buhmann, Nonadditivity of Optical and Casimir-Polder Potentials, Phys. Rev. Lett. 121, 83603 (2018).
- [5] H. J. Metcalf and P. van der Straten, Laser Cooling and Trapping (Springer-Verlag) (1999).
- [6] R. Wynands and S. Weyers, Atomic fountain clocks, Metrologia 42, 64 (2005).
- [7] A. D. Ludlow, M. M. Boyd, and J. Ye, Optical atomic clocks, Review of Modern Physics 87, 637–701 (2015).
- [8] M. S. Safronova, D. Budker, D. Demille, D. F. J. Kimball, A. Derevianko, and C. W. Clark, Search for new physics with atoms and molecules, Reviews of Modern Physics 90, 25008 (2018).
- [9] R. J. Rengelink, Y. van der Werf, R. P. Notermans, R. Jannin, K. S. Eikema, M. D. Hoogerland, and W. Vassen, Precision spectroscopy of helium in a magic wavelength optical dipole trap, Nature Physics 14, 1132– 1137 (2018), arXiv:1804.06693.
- [10] P. Asenbaum, C. Overstreet, M. Kim, J. Curti, and M. A. Kasevich, Atom-Interferometric Test of the Equivalence Principle at the 10-12 Level, Physical Review Letters 125, 191101 (2020), arXiv:2005.11624.
- [11] H. Stærkind, K. Jensen, J. H. Müller, V. O. Boer, E. T. Petersen, and E. S. Polzik, Precision Measurement of the Excited State Landé g-factor and Diamagnetic Shift of the Cesium D 2 Line, Physical Review X 13, 21036 (2023), arXiv:2208,00077.
- [12] X. Zheng, Y. R. Sun, J. J. Chen, W. Jiang, K. Pachucki, and S. M. Hu, Measurement of the Frequency of the 2 S 3 -2 P 3 Transition of He 4, Physical Review Letters 119, 263002 (2017).
- [13] R. Brown, S. Wu, J. Porto, C. Sansonetti, C. Simien, S. Brewer, J. Tan, and J. Gillaspy, Quantum interference and light polarization effects in unresolvable atomic lines: Application to a precise measurement of the 6,7Li D 2 lines, Physical Review A 87, 032504 (2013).
- [14] T. Peyrot, N. Sibalić, Y. R. Sortais, A. Browaeys, A. Sargsyan, D. Sarkisyan, I. G. Hughes, and C. S. Adams, Measurement of the atom-surface van der Waals interaction by transmission spectroscopy in a wedged nanocell, Physical Review A 100, 022503 (2019), arXiv:1905.02783.
- [15] E. Deist, J. A. Gerber, Y.-H. Lu, J. Zeiher, and D. M. Stamper-Kurn, Superresolution microscopy of optical fields using tweezer-trapped single atoms, Phys. Rev. Lett. 128, 083201 (2022).
- [16] A. P. Hilton, A. N. Luiten, and P. S. Light, Light-shift spectroscopy of optically trapped atomic ensembles, New Journal of Physics 22, 033042 (2020), arXiv:1911.02708.
- [17] C.-L. Hung, X. Zhang, L.-C. Ha, S.-K. Tung, N. Gemelke, and C. Chin, Extracting density-density correlations from in situ images of atomic quantum gases, New Journal of Physics 13, 075019 (2011).
- [18] Y. Wang, J. Zhao, X. Huang, L. Qiu, L. Ji, Y. Ma, Y. He, J. P. Sobol, and S. Wu, *Imaging Moving Atoms by Holographically Reconstructing the Dragged Slow Light*, Physical Review Applied 18, 014065 (2022),

- arXiv:2105.14832.
- [19] J. Zhao, Y. Wang, X. Huang, and S. Wu, Spectroscopic localization of atomic sample plane for precise digital holography, Optics Express, 18–22 (2022).
- [20] J. M. Higbie, L. E. Sadler, S. Inouye, A. P. Chikkatur, S. R. Leslie, K. L. Moore, and V. Savalli, Direct Nondestructive Imaging of Magnetization in a Spin-1 Bose-Einstein Gas, Physical Review Letters 95, 050401 (2005).
- [21] S. A. Aljunid, M. K. Tey, B. Chng, T. Liew, G. Maslennikov, V. Scarani, and C. Kurtsiefer, *Phase Shift of a Weak Coherent Beam Induced by a Single Atom*, Phys. Rev. Lett. 103, 153601 (2009).
- [22] M. Kohnen, P. G. Petrov, R. A. Nyman1, and E. A. Hinds, Minimally destructive detection of magnetically trapped atoms using frequency-synthesized light, New Journal of Physics 13, 085006 (2011).
- [23] M. Pototschnig, Y. Chassagneux, J. Hwang, G. Zumofen, A. Renn, and V. Sandoghdar, Controlling the Phase of a Light Beam with a Single Molecule, Physical Review Letters 107, 063001 (2011).
- [24] M. Fischer, B. Srivathsan, L. Alber, M. Weber, M. Sondermann, and G. Leuchs, Shifting the phase of a coherent beam with a 174Yb + ion: influence of the scattering cross section, Applied Physics B: Lasers and Optics 123, 48 (2017), arXiv:1609.08335.
- [25] B. Zhu, J. Cooper, J. Ye, and A. M. Rey, Light scattering from dense cold atomic media, Physical Review A 94, 023612 (2016).
- [26] A. B. Deb, J. Chung, and N. Kjærgaard, Dispersive detection of atomic ensembles in the presence of strong lensing, New Journal of Physics 22, 073017 (2020), arXiv:2002.10618.
- [27] S. Agarwal, E. Chaparro, D. Barberena, A. P. Orioli, G. Ferioli, S. Pancaldi, I. Ferrier-Barbut, A. Browaeys, and A. M. Rey, *Directional superradiance in a driven* ultracold atomic gas in free-space, arXiv, 43–47 (2024), arXiv:arXiv:2403.15556v1.
- [28] D. Gabor, Holography, 1948-1971, Proceedings of the IEEE 60, 655 (1972).
- [29] T. Latychevskaia, Phase retrieval for digital holography, Journal of the Optical Society of America A 36, 31 (2019).
- [30] J. P. Sobol and S. Wu, Imaging cold atoms with shotnoise and diffraction limited holography, New Journal of Physics 16, 093064 (2014).
- [31] D. Gabor, Theory of communication. Part 1: The analysis of information, Journal of the Institution of Electrical Engineers Part III: Radio and Communication Engineering 93, 429–441 (1946).
- [32] E. J. Heller, Time-dependent approach to semiclassical dynamics, The Journal of Chemical Physics 62, 1544– 1555 (1975).
- [33] J. E. Harvey, R. G. Irvin, and R. N. Pfisterer, Modeling physical optics phenomena by complex ray tracing, Optical Engineering 54, 035001 (2015).
- [34] J. N. Ashcraft and E. S. Douglas, An open-source gaussian beamlet decomposition tool for modeling astronomical telescopes, Proc. SPIE 11450, Modeling, Systems Engineering, and Project Management for Astronomy IX, 11450, 1 (2020), arXiv:2106.09162.
- [35] S. L. Braunstein, C. M. Caves, and G. J. Milburn, Generalized uncertainty relations: Theory, examples, and Lorentz invariance, Annals of Physics 247, 135 (1996),

- arXiv:9507004v1 [arXiv:quant-ph].
- [36] E. Cuche, F. Bevilacqua, and C. Depeursinge, *Digital holography for quantitative phase-contrast imaging*, Optics Letters **24**, 291 (1999).
- [37] P. Marquet, B. Rappaz, P. J. Magistretti, E. Cuche, Y. Emery, T. Colomb, and C. Depeursinge, Digital holographic microscopy: a noninvasive contrast imaging technique allowing quantitative visualization of living cells with subwavelength axial accuracy, Optics Letters 30, 468 (2005).
- [38] T. L. Nguyen, S. Pradeep, R. L. Judson-torres, J. Reed, M. A. Teitell, and T. A. Zangle, Quantitative Phase Imaging: Recent Advances and Expanding Potential in Biomedicine, ACS Nano 16, 11516 (2022).
- [39] For the notation conciseness, we may omit the x, y variables, or x, y, z variables, when expressing the complex and real fields.
- [40] S. Kadlecek, J. Sebby, R. Newell, and T. G. Walker, Nondestructive spatial heterodyne imaging of cold atoms, Optics Letters 26, 137 (2001).
- [41] L. D. Turner, K. F. E. M. Domen, and R. E. Scholten, Diffraction-contrast imaging of cold atoms, Physical Review A 72, 031403 (2005).
- [42] J. Smits, A. P. Mosk, and P. van der Straten, Imaging trapped quantum gases by off-axis holography, Optics Letters 45, 981 (2020), arXiv:1911.09590.
- [43] E. Altuntas and I. B. Spielman, Self-Bayesian Aberration Removal via Constraints for Ultracold Atom Microscopy, Phys. Rev. Res 3, 043087 (2021), arXiv:2108.07106.
- [44] I. Yamaguchi and T. ZHang, Phase-shifting digital holography, Optics Letters 22, 1268–1270 (1997).
- [45] R. G. Paxman, T. J. Schulz, and J. R. Fienup, Joint estimation of object and aberrations by using phase diversity, Journal of the Optical Society of America A 9, 1072 (1992).
- [46] X. Ou, R. Horstmeyer, C. Yang, and G. Zheng, Quantitative phase imaging via Fourier ptychographic microscopy, Optics Letters 38, 4845 (2013).
- [47] A. R. Perry, S. Sugawa, F. Salces-Carcoba, Y. Yue, and I. B. Spielman, Multiple-camera defocus imaging of ultracold atomic gases, Optics Express 29, 17029 (2021), arXiv:2102.08292.
- [48] E. N. Leith and J. Upatnieks, Reconstructed Wavefronts and Communication Theory*, Journal of the Optical Society of America 52, 1123 (1962).
- [49] P. Gao, G. Pedrini, and W. Osten, Structured illumination for resolution enhancement and autofocusing in digital holographic microscopy, Optics Letters 11, 090901 (2013).
- [50] C. Zuo, J. Li, J. Sun, Y. Fan, J. Zhang, L. Lu, R. Zhang, B. Wang, L. Huang, and Q. Chen, Transport of intensity equation: a tutorial, Optics and Lasers in Engineering 135, 106187 (2020).
- [51] The highly sensitive relation between the apparent OD and ϕ at the sample plane $z=z_A$ is exploited itself for holographic imaging of cold atoms, as in ref. [41] and more generally discussed in ref. [43]. Here, since we plan is to measure OD and ϕ , their relation cannot be assumed as a prior knowledge in general.
- [52] H. A. Ilhan, M. Doğar, and M. Özcan, in Practical Holography XXVII: Materials and Applications, Vol. 8644 (SPIE, 2013) pp. 77–87.
- [53] D. J. Brady, K. Choi, D. L. Marks, R. Horisaki, and

- S. Lim, Compressive Holography, Opt. Express 17, 13040 (2009).
- [54] Y. Zhang, H. Wang, Y. Wu, M. Tamamitsu, and A. Ozcan, Edge sparsity criterion for robust holographic autofocusing, Optics Letters 42, 3824 (2017).
- [55] X. Fan, J. J. Healy, and B. M. Hennelly, Investigation of sparsity metrics for autofocusing in digital holographic microscopy, Opt. Eng. 56, 053112 (2017).
- [56] Y. Wu, Y. Rivenson, Y. Zhang, Z. Wei, H. Günaydin, X. Lin, and A. Ozcan, Extended depth-of-field in holographic imaging using deep-learning-based autofocusing and phase recovery, Optica 5, 704 (2018).
- [57] B. Redding, M. A. Choma, and H. Cao, Speckle-free laser imaging using random laser illumination, Nature Photonics 6, 355 (2012).
- [58] G. Koren, F. Polack, and D. Joyeux, Iterative algorithms for twin-image elimination in in-line holography using finite-support constraints, Journal of the Optical Society of America A 10, 423 (1993).
- [59] S. O. Isikman, W. Bishara, S. Mavandadi, F. W. Yu, S. Feng, R. Lau, and A. Ozcan, Lens-free optical tomographic microscope with a large imaging volume on a chip, Proceedings of the National Academy of Sciences of the United States of America 108, 7296 (2011).
- [60] T. Latychevskaia and H.-w. Fink, Solution to the Twin Image Problem in Holography, Phys. Rev. Lett. 98, 233901 (2007).
- [61] G. E. Marti, R. B. Hutson, A. Goban, S. L. Campbell, N. Poli, and J. Ye, *Imaging Optical Frequencies with 100 muHz Precision and 1 . 1 mu m Resolution*, Physical Review Letters 120, 103201 (2018).
- [62] R. Li, Y. Wu, Y. Rui, B. Li, Y. Jiang, L. Ma, and H. Wu, Absolute Frequency Measurement of Li 6 D Lines with khz-Level Uncertainty, Physical Review Letters 124, 063002 (2020).
- [63] L. Chomaz, L. Corman, T. Yefsah, R. Desbuquois, and J. Dalibard, Absorption imaging of a quasi-twodimensional gas: a multiple scattering analysis, New Journal of Physics 14, 055001 (2012).
- [64] S. Kuhr, Special Topic: Cold Atoms Quantum-gas microscopes: a new tool for cold-atom quantum simulators, Nature Science Review 3, 170-172 (2016).
- [65] G. Zheng, R. Horstmeyer, and C. Yang, Wide-field, high-resolution Fourier ptychographic microscopy, Nature Photonics 7, 739 (2013).
- [66] G. Zheng, X. Ou, R. Horstmeyer, and C. Yang, Characterization of spatially varying aberrations for wide fieldof-view microscopy, Optics Express 21, 15131 (2013).
- [67] K. Park, T. Kong, T. D. Yang, and Y. Choi, Measurement of multiple phase maps for wide-area aberration correction by switchable optical configuration, Optics Express 29, 41894 (2021).
- [68] J. P. Sobol, Imaging cold atoms with shot-noise and diffraction limited holography, Ph.D. thesis, Swansea University (2015).
- [69] G.-z. Yang, B.-z. Dong, B.-y. Gu, J.-y. Zhuang, and O. K. Ersoy, Gerchberg–Saxton and Yang–Gu algorithms for phase retrieval in a nonunitary transform system: a comparison, Applied Optics 33, 209 (1994).
- [70] R. Meppelink, R. A. Rozendaal, S. B. Koller, J. M. Vogels, and P. V. D. Straten, Thermodynamics of Bose-Einstein-condensed clouds using phase-contrast imaging, Physical Review A 81, 053632 (2010).
- [71] G. Reinaudi, T. Lahaye, Z. Wang, and D. Guéry-Odelin,

- Strong saturation absorption imaging of dense clouds of ultracold atoms, Optics Letters **32**, 3143 (2007), arXiv:0707.2930.
- [72] D. A. Steck, Rubidium 87 D Line Data, http://steck.us/alkalidata (revision 2.2.1, 21 November 2019)..
- [73] W. Alt, An objective lens for efficient fluorescence detection of single atoms, Optik (Jena) 113, 142–144 (2002), arXiv:0108058 [physics].
- [74] X. Li, F. Zhou, M. Ke, P. Xu, X.-D. He, J. Wang, and M.-S. Zhan, High-resolution ex vacuo objective for cold atom experiments, Applied Optics 57, 7584 (2018).
- [75] G. D. Bruce, E. Haller, B. Peaudecerf, D. A. Cotta, M. Andia, S. Wu, M. Y. Johnson, B. W. Lovett, and S. Kuhr, Sub-Doppler laser cooling of 40K with Raman gray molasses on the D2 line, Journal of Physics B: Atomic, Molecular and Optical Physics 50, 095002 (2017), arXiv:1612.04583.
- [76] By comparing the shot-to-shot data between different samples, noticeable $\bar{\beta}$ —correlations can be found at a level consistent with the frequency noise of our saturation-spectrum-locked cateye laser (Moglabs CEL) at 100 kHz level. The relative phase-angle variations are close to the photon-shot-noise limit set by Eq. (9).
- [77] R. Bachelard, N. Piovella, W. Guerin, and R. Kaiser, Collective effects in the radiation pressure force, Phys. Rev. A 94, 033836 (2016).
- [78] P. C. Bons, R. De Haas, D. De Jong, A. Groot, and P. Van Der Straten, Quantum Enhancement of the Index of Refraction in a Bose-Einstein Condensate, Phys. Rev. Lett. 116, 173602 (2016).
- [79] C. Gross and I. Bloch, Quantum simulations with ultracold atoms in optical lattices., Science 357, 995–1001 (2017).
- [80] W. S. Bakr, J. I. Gillen, A. Peng, S. Fölling, and M. Greiner, A quantum gas microscope for detecting single atoms in a Hubbard-regime optical lattice, Nature 462, 74–77 (2009), arXiv:0908.0174.
- [81] J. F. Sherson, C. Weitenberg, M. Endres, M. Cheneau, I. Bloch, and S. Kuhr, Single-Atom Resolved Fluorescence Imaging of an Atomic Mott Insulator, Nature 467, 68 (2010), arXiv:arXiv:1006.3799v2.
- [82] D. Okuno, Y. Amano, K. Enomoto, N. Takei, and Y. Takahashi, Schemes for nondestructive quantum gas microscopy of single atoms in an optical lattice, New J. Phys. 22, 013041 (2020).
- [83] K. D. Nelson, X. Li, and D. S. Weiss, *Imaging single atoms in a three-dimensional array*, Nature Physics 3, 556 (2007).
- [84] D. Barredo, V. Lienhard, S. de Léséleuc, T. Lahaye, and A. Browaeys, Synthetic three-dimensional atomic structures assembled atom by atom, Nature 561, 79–82 (2018), arXiv:1712.02727.
- [85] I. B. Spielman, W. D. Phillips, and J. V. Porto, Mott-Insulator Transition in a Two-Dimensional Atomic Bose Gas, Phys. Rev. Lett. 98, 080404 (2007).
- [86] A. Greenbaum, W. Luo, T. W. Su, Z. Göröcs, L. Xue, S. O. Isikman, A. F. Coskun, O. Mudanyali, and A. Ozcan, *Imaging without lenses: Achievements and remain*ing challenges of wide-field on-chip microscopy, Nat. Methods 9, 889 (2012).
- [87] K. De Haan, Y. Rivenson, Y. Wu, and A. Ozcan, Deep-Learning-Based Image Reconstruction and Enhance-

- ment in Optical Microscopy, Proc. IEEE 108, 2949575 (2020).
- [88] J. Park, D. J. Brady, G. Zheng, L. Tian, and L. Gao, Review of bio-optical imaging systems with a high spacebandwidth product, Adv. Photonics 3, 044001 (2021).
- [89] X. Kong, A. Markmann, and V. S. Batista, Time-Sliced Thawed Gaussian Propagation Method for Simulations of Quantum Dynamics, Journal of Physical Chemistry A 120, 3260–3269 (2016).
- [90] N. G. Worku and H. Gross, Gaussian pulsed beam decomposition for propagation of ultrashort pulses through optical systems, Journal of the Optical Society of America A 37, 98 (2020).
- [91] T. Legrand, F. R. Winkelmann, W. Alt, D. Meschede, A. Alberti, and C. A. Weidner, Three-dimensional imaging of single atoms in an optical lattice via helical pointspread-function engineering, Physical Review A 109, 033304 (2024), arXiv:2312.05341.
- [92] S. Diego, S. Diego, M. E. Mossman, R. A. Corbin, M. M. Forbes, and P. Engels, Atom Interferometric Imaging of Differential Potentials Using an Atom Laser, Physical Review Letters 130, 263402 (2023).
- [93] L. Ji, Y. He, Q. Cai, Z. Fang, Y. Wang, L. Qiu, L. Zhou, S. Wu, and S. Grava, Superradiant Detection of Microscopic Optical Dipolar Interactions, Phys. Rev. Lett. 131, 253602 (2023).
- [94] J. Rui, D. Wei, A. Rubio-Abadal, S. Hollerith, J. Zeiher, D. M. Stamper-Kurn, C. Gross, and I. Bloch, A subradiant optical mirror formed by a single structured atomic layer, Nature 583, 369–374 (2020), arXiv:2001.00795.
- [95] A. B. Deb and N. Kjærgaard, Observation of Pauli blocking in light scattering from quantum degenerate fermions, Science (80-.). 374, 972–975 (2021).
- [96] Y. K. Lu, Y. Margalit, and W. Ketterle, Bosonic stimulation of atom-light scattering in an ultracold gas, Nature Physics 19, 210–214 (2022).
- [97] K. Srakaew, P. Weckesser, S. Hollerith, D. Wei, D. Adler, I. Bloch, and J. Zeiher, A subwavelength atomic array switched by a single Rydberg atom, Nature Physics 10, 1038 (2023), 2207.09383.
- [98] J. E. Lye, J. J. Hope, and J. D. Close, Nondestructive dynamic detectors for Bose-Einstein condensates, Phys. Rev. A 67, 043609 (2003).
- [99] J. Miao, P. Charalambous, J. Kirz, and D. Sayre, Extending the methodology of X-ray crystallography to non-crystalline specimens, Nature 400, 342 (1999).
- [100] M. Babiker, D. L. Andrews, V. E. Lembessis, M. Hamamda, P. Pillet, Y. Yin, and Y. Xia, Sisyphus cooling in a continuously loaded trap, New Journal of Physics 15, 093012 (2013).
- [101] A. La Rooij, C. Ulm, E. Haller, and S. Kuhr, A comparative study of deconvolution techniques for quantum-gas microscope images, New Journal of Physics 25, 083036 (2023), arXiv:2207.08663.
- [102] Y. Castin, in COHERENT ATOMIC MATTER WAVES, LES HOUCHES SUMMER SCHOOL SES-SION, Vol. 72, edited by R. Kaiser, C. Westbrook, and F. David (NATO, Adv Study Inst, 2001) pp. 5–136.
- [103] D. P. Kingma and J. L. Ba, Adam: A method for stochastic optimization, 3rd International Conference on Learning Representations, ICLR 2015 - Conference Track Proceedings, 1–15 (2015), arXiv:1412.6980.